This is a repository copy of *A quantitative comparison of amplitude versus intensity interferometry for astronomy*.

White Rose Research Online URL for this paper:
https://eprints.whiterose.ac.uk/186309/

Version: Published Version

Article:

New Journal of Physics

The open access journal at the forefront of physics

PAPER

A quantitative comparison of amplitude versus intensity interferometry for astronomy

Manuel Bojer[1],[*] ⓘ, Zixin Huang[2],[3], Sebastian Karl[1] ⓘ, Stefan Richter[1],[4] ⓘ, Pieter Kok[2] and Joachim von Zanthier[1],[4] ⓘ

[1] Institut für Optik, Information und Photonik, Friedrich-Alexander-Universität Erlangen-Nürnberg, 91058 Erlangen, Germany
[2] Department of Physics & Astronomy, University of Sheffield, United Kingdom
[3] Centre for Engineered Quantum Systems, Department of Physics and Astronomy, Macquarie University, NSW 2109, Australia
[4] Erlangen Graduate School in Advanced Optical Technologies (SAOT), Germany
[*] Author to whom any correspondence should be addressed.

E-mail: manuelbojer6@gmail.com, zixin.huang@sheffield.ac.uk, seb.karl@fau.de, stefan.michael.richter@fau.de, p.kok@sheffield.ac.uk and joachim.vonzanthier@fau.de

Keywords: quantum metrology, imaging astronomical objects, (quantum) Fisher information

Abstract

Astronomical imaging can be broadly classified into two types. The first type is amplitude interferometry, which includes conventional optical telescopes and very large baseline interferometry (VLBI). The second type is intensity interferometry, which relies on Hanbury Brown and Twiss-type measurements. At optical frequencies, where direct phase measurements are impossible, amplitude interferometry has an effective numerical aperture that is limited by the distance from which photons can coherently interfere. Intensity interferometry, on the other hand, correlates only photon fluxes and can thus support much larger numerical apertures, but suffers from a reduced signal due to the low average photon number per mode in thermal light. It has hitherto not been clear which method is superior under realistic conditions. Here, we give a comparative analysis of the performance of amplitude and intensity interferometry, and we relate this to the fundamental resolution limit that can be achieved in any physical measurement. Using the benchmark problem of determining the separation between two distant thermal point sources, e.g., two adjacent stars, we give a short tutorial on optimal estimation theory and apply it to stellar interferometry. We find that for very small angular separations the large baseline achievable in intensity interferometry can more than compensate for the reduced signal strength. We also explore options for practical implementations of very large baseline intensity interferometry (VLBII).

1. Introduction

Imaging takes a primary place in the instrumentarium of science. It has been responsible for some of the most dramatic discoveries, from Galileo's observations of the orbits of Jupiter's moons that were essential in overturning the Ptolemaic world view, to the imaging of the black hole in M87 by the Event Horizon Telescope (EHT) Collaboration that provided direct evidence for the existence of black holes and a stunning confirmation of Einstein's general relativity [1]. In microscopy, imaging has revolutionised our understanding of the natural world many times over, from Antonie van Leeuwenhoek's discovery of micro-organisms to superresolution imaging of large molecules.

It is well-known that the wave nature of light places a limit on the resolution that can be achieved in an image. The maximum resolution for a direct imaging system is given by Abbe's limit, which is determined by the wavelength of the light divided by the numerical aperture of the imaging apparatus [2]. Consequently, much of the efforts in producing better images in stellar astronomy has been in creating telescopes with larger numerical apertures. The Extremely Large Telescope (ELT) in Chile is currently the largest optical and infrared telescope with a compound mirror of 39.3 m in diameter [3]. Moreover, the

GRAVITY Collaboration at the Very Large Telescope (VLT) aims to collect and interfere optical signals from a number of telescopes, achieving an effective numerical aperture on the order of 100 m [4]. The Center for High Angular Resolution Astronomy (CHARA) collects coherently infrared light from six telescopes of 1 m diameter, e.g., in the MIRC-X instrument, spanning an effective numerical aperture of 300 m [5, 6]. Even more impressive, the EHT Collaboration used an array of existing telescopes all over the globe to create an effective numerical aperture the size of the Earth, with a resolution better than 20 μas. However, the latter method is restricted to lower frequency signals (the observed wavelength was 1.3 mm), since the telescopes have to be phase synchronized, i.e., each telescope must make a phase measurement of the electromagnetic field, in order to combine the many signals into a single coherent image [1]. At higher frequencies, detectors are not phase stable and fast enough, and we must find alternative ways to improve the resolution.
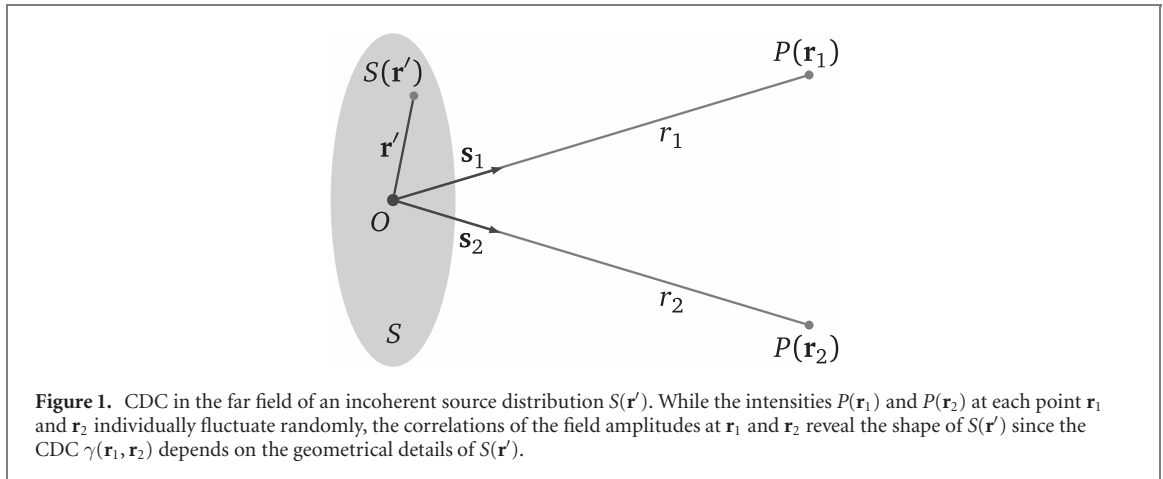
Recently, Nair and Tsang discovered that Abbe's diffraction limit is an artefact of the imaging system [7], and that in principle one can construct an imaging apparatus (with a finite numerical aperture) that can resolve two incoherent point sources at distances much lower than the wavelength of the light. Crucially, this does not require manipulation of the object, as is common in many modern super-resolution techniques [8]. The reason is that the quantum state of light contains the information about the separation of the sources, but in the detection plane of the imaging system this information is enclosed in the phase instead of the intensity. Changing the measurement configuration can unlock this information in principle. It was subsequently shown by Lupo *et al* that imaging of N incoherent point sources can be achieved equally optimally as in [7] using again only linear optics and phase sensitive interferometry [9].

Working towards a less involved and more general-purpose but still near-optimal imaging protocol for objects emitting light incoherently, Pearce *et al* developed a method for estimating the complex degree of coherence (CDC) of the light emitted by the object [10]. The CDC can be used to reconstruct the intensity profile in the source plane via a simple Fourier transform—the well-known Van Cittert–Zernike theorem—which for a thermal light source contains the complete information about the source distribution. This method was demonstrated experimentally by Howard *et al* [11]. Technical challenges remain, as for the protocol the fields have to be recorded at different positions and superposed phase coherently during the detection, for which the detector positions must be known and kept fixed to within a fraction of the wavelength of the light.

Circumventing the need for phase coherence over large distances at optical frequencies is another option for beating the diffraction limit. Hanbury Brown and Twiss famously developed optical intensity interferometry, using a pair of 6.5 m telescopes acting as light detectors separated by up to 188 m [12]. The method is not sensitive to the absolute phase of the fields at the location of the detectors, so the effective numerical aperture of the interferometer was on the order of 200 m. In this way, Hanbury Brown and Twiss (HBT) successfully measured the diameter of Sirius A and many other stellar diameters [13, 14]. Yet, a downside of HBT intensity interferometry is the low mode occupancy of thermal light, which means that recording a two-photon event in a single optical mode is exceedingly more rare as compared to a single-photon detection as in amplitude interferometry. The average photon number at frequency ω in a single thermal mode characterized by a wave vector $\boldsymbol{k}$ and polarisation s is given by the degeneracy parameter $\delta = (e^{\hbar\omega/k_B T} - 1)^{-1}$, where k_B is Boltzmann's constant and T is the temperature of the light source [15]. For light at a wavelength of 600 nm from the surface of a star at a temperature of 5000 K we have $\delta \approx 8 \times 10^{-3}$, whereas for near infrared wavelengths (900 nm) at the same temperature the degeneracy parameter is $\delta \approx 0.04$. This value is important for both interferometric methods, with the signal scaling linearly in δ for amplitude interferometry and quadratically in δ for intensity interferometry.

However, δ is not the only relevant factor in extracting the information about the source separation in both interferometric methods. Of equal importance is the numerical aperture of the interferometer which at optical frequencies can be larger by a factor of 100 and more for modern intensity interferometers with respect to even today's largest amplitude interferometers. As it turns out, this advantage can more than compensate for the drawback of low degeneracy parameters in the optical domain, in particular considering very small stellar separations.

Since δ is unfavourable for HBT interferometry, and because timing resolution and efficiencies of the detectors at the time of the original HBT experiments were restricted, intensity interferometry was largely abandoned in the 1970s in favour of amplitude interferometry [16]. Yet, modern detector technology has considerably advanced efficiencies, timing capabilities, data processing, and synchronisation, and thus has enabled a new resurgence of HBT experiments with the goal of achieving improved resolution in astronomy. Recently, photon bunching, i.e., the temporal auto-correlation of photons, was measured with good signal-to-noise ratio for light from an artificial black body and the Sun [17, 18], from well-controlled laboratory sources [19, 20], as well as from distant stars [21–26], and first small baseline HBT experiments were carried out aiming to resolve true stars by use of spatial single photon [27, 28] or intensity [29, 30] cross-correlations. For a recent review of stellar intensity interferometry, see Dravins [31].

Figure 1. CDC in the far field of an incoherent source distribution $S(\mathbf{r}')$. While the intensities $P(\mathbf{r}_1)$ and $P(\mathbf{r}_2)$ at each point $\mathbf{r}_1$ and $\mathbf{r}_2$ individually fluctuate randomly, the correlations of the field amplitudes at $\mathbf{r}_1$ and $\mathbf{r}_2$ reveal the shape of $S(\mathbf{r}')$ since the CDC $\gamma(\mathbf{r}_1, \mathbf{r}_2)$ depends on the geometrical details of $S(\mathbf{r}')$.

For thermal light sources like stars, one method of imaging the object of interest is knowing the CDC $\gamma(\mathbf{r}_1, \mathbf{r}_2)$, which measures the correlations between the electric field amplitudes at positions $\mathbf{r}_1$ and $\mathbf{r}_2$ in the far field of the object [15]:

$$\gamma(\mathbf{r}_1, \mathbf{r}_2) = \frac{\langle E^*(\mathbf{r}_1)\, E(\mathbf{r}_2)\rangle}{\sqrt{\langle E|(\mathbf{r}_1)|^2\rangle \langle |E(\mathbf{r}_2)|^2\rangle}}, \tag{1}$$

where $\langle E^*(\mathbf{r}_1)E(\mathbf{r}_2)\rangle = G^{(1)}(\mathbf{r}_1, \mathbf{r}_2)$ is the first-order correlation function of the electric field at positions $\mathbf{r}_1$ and $\mathbf{r}_2$. The CDC is related to the source (intensity) distribution $S(\mathbf{r}')$ via the Van Cittert–Zernike theorem [32, 33]

$$\gamma(\mathbf{r}_1, \mathbf{r}_2) = \frac{e^{ik(r_2 - r_1)}}{S_0} \int_S d\mathbf{r}'\, S(\mathbf{r}')e^{-ik(\mathbf{s}_2 - \mathbf{s}_1)\cdot\mathbf{r}'}, \tag{2}$$

where S_0 denotes the integrated source intensity and $k = 2\pi/\lambda$, with λ the wavelength of the light (see figure 1). Further, $\mathbf{s}_1$ and $\mathbf{s}_2$ denote the unit vectors in the direction of $\mathbf{r}_1$ and $\mathbf{r}_2$. Hence, estimating $\gamma(\mathbf{r}_1, \mathbf{r}_2)$ in the far field allows for the reconstruction of the source distribution $S(\mathbf{r}')$. All of the methods we are about to discuss in this paper rely on estimating γ. For the phase sensitive techniques based on amplitude interferometry, which we call $G^{(1)}$ methods, one has access to the complex quantity γ. On the other hand, for intensity interferometry, which we call $G^{(2)}$ methods, we have access only to the modulus of the CDC $|\gamma|$ via the normalized second-order correlation function $g^{(2)}(\mathbf{r}_1, \mathbf{r}_2) = 1 + |\gamma(\mathbf{r}_1, \mathbf{r}_2)|^2$ [15]. For simple objects such as resolving the diameter of a star, no involved phase information is needed and it is sufficient to measure the absolute value of the CDC. For more complex objects, however, the phase information of the CDC is essential since it is required for the reconstruction of the source intensity distribution via the Van Cittert–Zernike theorem in equation (2). The $G^{(2)}$ methods can in principle overcome this difficulty by using well-established methods of phase recovery. There are several candidates, such as the Cauchy–Riemann approach [34, 35], Gerchberg–Saxon algorithms [36–39], and ptychographical intensity interferometry [40, 41].

In this paper, we analyse quantitatively the relative strengths of the different imaging methods described above using the (quantum) Fisher information (FI). The latter is a well-established measure from estimation theory to quantify the amount of information one can extract from the electromagnetic field with a given (optimal) measurement. The measure takes into account both the limits induced by the wave nature and the particle nature of light, i.e., the Abbe limit and shot-noise, and goes beyond a mere signal-to-noise ratio analysis [42]. We distinguish between (i) direct (Galilean) imaging using traditional phase interferometry by means of lenses and telescopes like the ELT, (ii) Tsang's small numerical aperture optimal imaging methodology [spatial mode demultiplexing (SPADE)], (iii) large aperture optimal interferometry like GRAVITY or CHARA, and (iv) imaging based on intensity interferometry such as HBT. The first three methods require access to the phase in the optical signal, including establishing a constant phase across the entire mirror of a telescope using active and adaptive optics, while the latter does not. We consider the theoretical limits to the resolution for the various interferometric methods taking into account the different achievable detector sizes as well as detector separations. For an easier comparison of the methods, we will consider the separation of two incoherent thermal point sources of potentially unequal brightness as our benchmark problem. Other important problems such as diameter estimation require more refined estimation techniques but do not lead to new bounds.

The paper is organised as follows. In section 2 we present a short introduction to the (quantum) FI. In section 3 we review the various phase-coherent imaging methods, including traditional imaging and the new quantum imaging techniques, and examine some of their practical limitations. In section 4 we discuss intensity interferometry for imaging, and compare it in section 5 to the amplitude interferometry techniques of section 3. In section 6 we consider possible applications of intensity interferometry. We present our conclusions in section 7.

2. Tutorial: Fisher information

We provide a brief tutorial on the use of estimation theory in imaging and how to apply this to optimal—in a fundamental quantum mechanical sense—astronomical measurements. We can consider imaging problems as multi-parameter estimation problems. For example, the CDC $\gamma(\mathbf{r}_1, \mathbf{r}_2)$ for each pair of positions $\mathbf{r}_1, \mathbf{r}_2$ in the imaging plane is given by two parameters (e.g., the modulus $|\gamma|$ and its phase), and estimation theory can tell us what is the physical limit on the error in the parameter, given a particular measurement setup. This bound, the Cramér–Rao bound, is determined by the Fisher information (FI), i.e., the average information that is extracted in a measurement of the parameter. The *quantum* Fisher information (QFI) is the FI of the optimal quantum measurement, and is an intrinsic quantity of the quantum state (just like the entropy of a system is determined by its state and not how it is measured).

2.1. Fisher information

When we measure a physical quantity, we are interested not only in the value of that quantity, but also in the expected error in the measurement, typically in the form of the mean square error. Moreover, the quantity may not be measured directly, but rather is estimated indirectly based on the measurement of an observable that is related to it. As an example, consider the estimation of a phase difference θ between two arms of an interferometer. We cannot measure θ directly. Instead, we measure the photocurrent in the detectors at the output of the interferometer, and the measured currents allow us to infer a value of θ. This is done via an estimator $\hat{\theta}(\mathbf{x})$, which is a function of the recorded data $\mathbf{x}$. Here, the data consists of the N different measured photocurrents $\mathbf{x} = (M_1, \ldots, M_N)$. A nontrivial question is then how we determine the mean square error $\sigma_{\hat{\theta}}^2$ in θ. It will be related to the variance σ_M^2 in the measured photocurrents according to the well-known error propagation formula

$$\sigma_{\hat{\theta}}^2 = \frac{\sigma_M^2}{|\mathrm{d}\langle M \rangle / \mathrm{d}\theta|^2}, \tag{3}$$

where $\langle M \rangle$ is the expectation value of the photocurrents. The quantity $\sigma_{\hat{\theta}}^2$ may be difficult to calculate directly due to the derivative $\mathrm{d}\langle M \rangle / \mathrm{d}\theta$, and considerable effort has been spent to derive attainable lower bounds on $\sigma_{\hat{\theta}}^2$. To this end, we define the FI $F(\theta)$ as a functional of the probability distribution $p(x|\theta)$ over the possible measurement outcomes x in the experiment
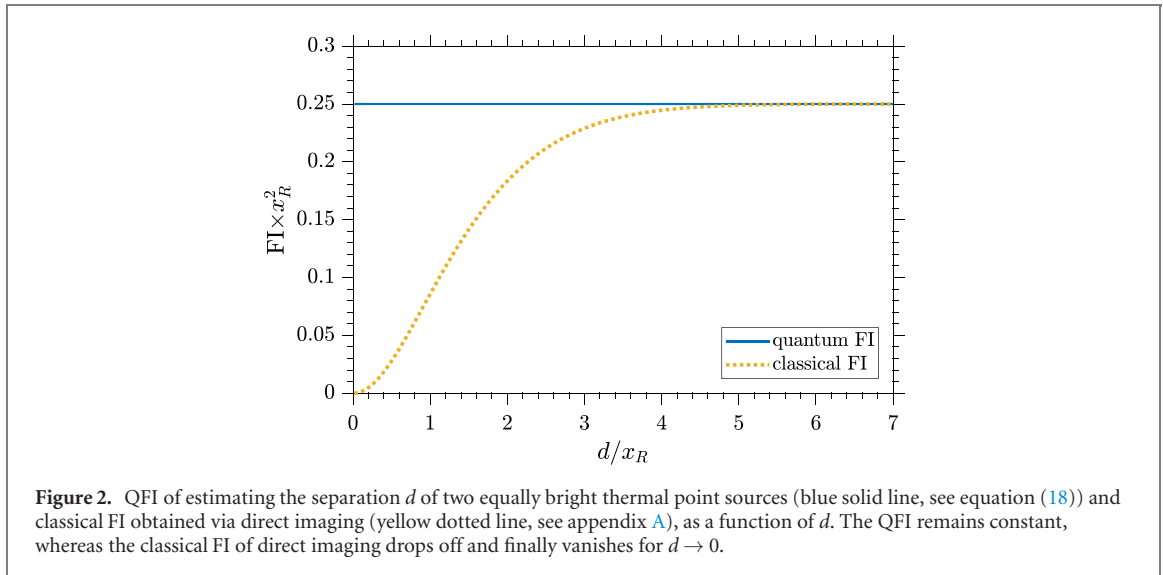
$$F(\theta) = \sum_x p(x|\theta) \left[\frac{\partial \log p(x|\theta)}{\partial \theta} \right]^2. \tag{4}$$

It is useful to think of the FI as the average of the square of the so-called logarithmic derivative $\partial \log p(x|\theta)/\partial\theta$. The logarithm translates products of probabilities of independent events into a sum required to make the information additive: when we make two independent measurements of the system the information gained should double. Furthermore, the derivative with respect to the parameter θ enters because the more a probability distribution changes as we change θ, the more information we expect to gain.

Given a model of the experiment, we can often determine $p(x|\theta)$ relatively easily, and by extension calculate $F(\theta)$. The mean square error $\sigma_{\hat{\theta}}^2$ is then bounded by the FI and the number N of statistically independent, identical repetitions of the experiment via

$$\sigma_{\hat{\theta}}^2 \geqslant [NF(\theta)]^{-1}. \tag{5}$$

This is the celebrated Cramér–Rao bound (CRB) on the precision with which we can estimate θ. It assumes that the estimator is unbiased. In imaging and stellar interferometry applications the parameter θ may be the separation between two distant point sources, a stellar diameter, or the magnitude/phase of the CDC, among many others. The bound is generally attainable for a single parameter θ using the maximum likelihood estimator $\hat{\theta}_{\mathrm{ML}}(\mathbf{x})$ [43]. If instead of a single parameter a parameter tuple $\boldsymbol{\theta} = (\theta_1, \ldots, \theta_n)^\top$ is to

Figure 2. QFI of estimating the separation d of two equally bright thermal point sources (blue solid line, see equation (18)) and classical FI obtained via direct imaging (yellow dotted line, see appendix A), as a function of d. The QFI remains constant, whereas the classical FI of direct imaging drops off and finally vanishes for $d \to 0$.

be estimated, the logarithmic derivatives in equation (4) are taken with respect to two of the n parameters. The FI then becomes a matrix

$$[F(\boldsymbol{\theta})]_{jk} = \sum_x p(x|\boldsymbol{\theta}) \left[\frac{\partial \log p(x|\boldsymbol{\theta})}{\partial \theta_j} \right] \left[\frac{\partial \log p(x|\boldsymbol{\theta})}{\partial \theta_k} \right], \tag{6}$$

and equation (5) becomes a matrix bound on the covariance matrix of the parameters

$$\mathrm{Cov}(\boldsymbol{\theta}) \succeq \frac{1}{N} [F^{-1}(\boldsymbol{\theta})], \tag{7}$$

meaning that $\mathrm{Cov}(\boldsymbol{\theta}) - F^{-1}(\boldsymbol{\theta})/N$ is a positive semidefinite matrix. This leads directly to a bound on the variances of the single parameters θ_j

$$\mathrm{Var}(\theta_j) = [\mathrm{Cov}(\boldsymbol{\theta})]_{jj} \geqslant \frac{1}{N} [F^{-1}(\boldsymbol{\theta})]_{jj}. \tag{8}$$

Using, for example, a maximum likelihood estimator, this CRB can be saturated.

Given a particular form of the point spread function (PSF), one can calculate the FI of direct imaging the separation d between two equally bright sources [44]. For a Gaussian PSF with variance x_R^2 it is calculated in appendix A. The result is shown in figure 2 (yellow dotted curve). As can be seen from the figure, for $d \gg x_R$ the FI is a constant and equal to $\frac{1}{4} x_R^{-2}$, however, it rapidly approaches zero as d drops below x_R. This phenomenon, dubbed the 'Rayleigh curse', means that estimation becomes increasingly difficult when d becomes smaller than x_R. Thus, estimation theory provides a rigorous foundation of the well-known Rayleigh criterion for image resolution.

2.2. Quantum Fisher information

While the FI in classical estimation theory is a functional of the conditional probability distribution over the measurement outcomes given the value of the parameter θ, in quantum estimation theory this becomes a functional of the quantum mechanical density operator describing the state of light. Two things should be noted: first, the density operator does not include any measurement outcomes, which instead are determined by the Hermitian observable that is measured, and second, the logarithmic derivative of an operator is not uniquely defined, giving rise to a certain amount of freedom in choosing the QFI.

To define the QFI, we replace the probability distribution $p(x|\theta)$ with the density operator $\rho(\theta)$, and we construct the so-called symmetric logarithmic derivative operator L_θ by solving the Lyapunov equation

$$\partial_\theta \rho = \frac{1}{2} \left(L_\theta \rho + \rho L_\theta \right), \tag{9}$$

where $\partial_\theta \rho$ is the derivative of $\rho(\theta)$ with respect to θ. The QFI then becomes

$$F_Q(\theta) = \mathrm{Tr} \left[\rho L_\theta^2 \right]. \tag{10}$$

Another way of arriving at equation (10) is by starting from the FI defined in equation (4), rewriting the probability distribution via Born's rule in terms of the measured observable and maximizing over all

possible measurement observables. This means, the QFI is the maximum information about θ, gained with an optimal measurement, such that $F_Q(\theta) \geqslant F(\theta)$.

The difficulty in calculating F_Q is typically due to finding a closed form of the symmetric logarithmic derivative L_θ. The quantum CRB on the mean square error in θ becomes

$$\sigma_\theta^2 \geqslant [NF(\theta)]^{-1} \geqslant [NF_Q(\theta)]^{-1}, \tag{11}$$

where the optimal measurement is constructed on the eigenbasis of L_θ. The bound is again attainable for a single parameter. Note that the QFI gives the ultimate precision with which the parameter θ can be estimated. It includes all sources of noise going along with the quantum state ρ, e.g., vacuum fluctuations or shot-noise in the case of a quantized light field. However, sources of noise coming from the detection of the quantum state ρ, e.g., detector imperfections are not included.

Imaging generally involves multiple parameters. For example, even the CDC for two positions in the imaging plane has two independent parameters, e.g., the magnitude and the phase of γ. We therefore extend the QFI to the symmetric matrix

$$[F_Q(\boldsymbol{\theta})]_{jk} = \mathrm{Tr}\left[\frac{1}{2}\rho\{L_j, L_k\}\right], \tag{12}$$

where the parameters are given by $\{\theta_j\}$, and each operator L_j is defined according to equation (9) with respect to the corresponding parameter θ_j. An analytic expression for the quantum Fisher information matrix (QFIM) reveals the dependency of estimation errors on different parameters, but is usually hard to compute and relies on finding a closed form of the symmetric logarithmic derivatives L_j. Usual approaches, relying on analytic matrix diagonalization, assume a representation of the density matrix in an orthogonal basis [45] or even in its eigenbasis [46]. Recently, a nonorthogonal-basis approach [47, 48] was used to find a general analytic expression for the QFIM, which relies on matrix inversion via determining the general solution of the associated Lyapunov equations [49].

Once the QFIM is known, the quantum CRB is a matrix bound on the covariance matrix over the parameters

$$\mathrm{Cov}(\boldsymbol{\theta}) \succeq \frac{1}{N}[F^{-1}(\boldsymbol{\theta})] \succeq \frac{1}{N}[F_Q^{-1}(\boldsymbol{\theta})]. \tag{13}$$

For the variances of the different parameters, the bound implies

$$\mathrm{Var}(\theta_j) = [\mathrm{Cov}(\boldsymbol{\theta})]_{jj} \geqslant \frac{1}{N}[F^{-1}(\boldsymbol{\theta})]_{jj} \geqslant \frac{1}{N}[F_Q^{-1}(\boldsymbol{\theta})]_{jj}. \tag{14}$$

Unfortunately, the matrix bound is no longer tight in general. It is easy to see that this must be the case when the operators L_j and L_k are incompatible, i.e., do not commute. Then it is impossible to design a measurement observable that is optimal for both θ_j and θ_k. This is a complication that we generally need to take into account, since the optimal measurement observables for, e.g., the phase and magnitude of the CDC are indeed incompatible. For a recent review on the QFI and the fundamentals of quantum estimation theory, see Sidhu and Kok [50].

In their seminal work [44], Tsang, Nair and Lu showed that the Rayleigh limit for imaging can be avoided if we exploit more general measurement strategies. They demonstrated that the QFI for the separation between two weak thermal point sources with equal intensities is constant and independent of the value of the separation, i.e., $F_Q(d) = \frac{1}{4}x_R^{-2}$ (see equation (18) and blue solid line in figure 2), whereas the classical FI of direct imaging vanishes as the separation between the point sources approaches zero (see appendix A and yellow dotted line in figure 2). This means that there is still a finite amount of information about the point source separation in the quantum state of light, even though the standard classical measurement does not have access to it.

In what follows, we treat the optimal measurement in more detail. We consider two thermal point sources emitting freely propagating photons into the far field. The sources are placed at positions $\boldsymbol{z}_1$ and $\boldsymbol{z}_2$ along the z-axis around a centroid position $\boldsymbol{z}_0$ and separated by a distance d (see figure 3). In the case of thermal light sources, the average photon number per mode is usually very small, which allows us to truncate the photonic state of appendix B after the one-photon state. Under the assumption that the overlap function $\eta(\boldsymbol{a})$ (see equation (46) in appendix B) is real and symmetric, the QFIM for estimating the
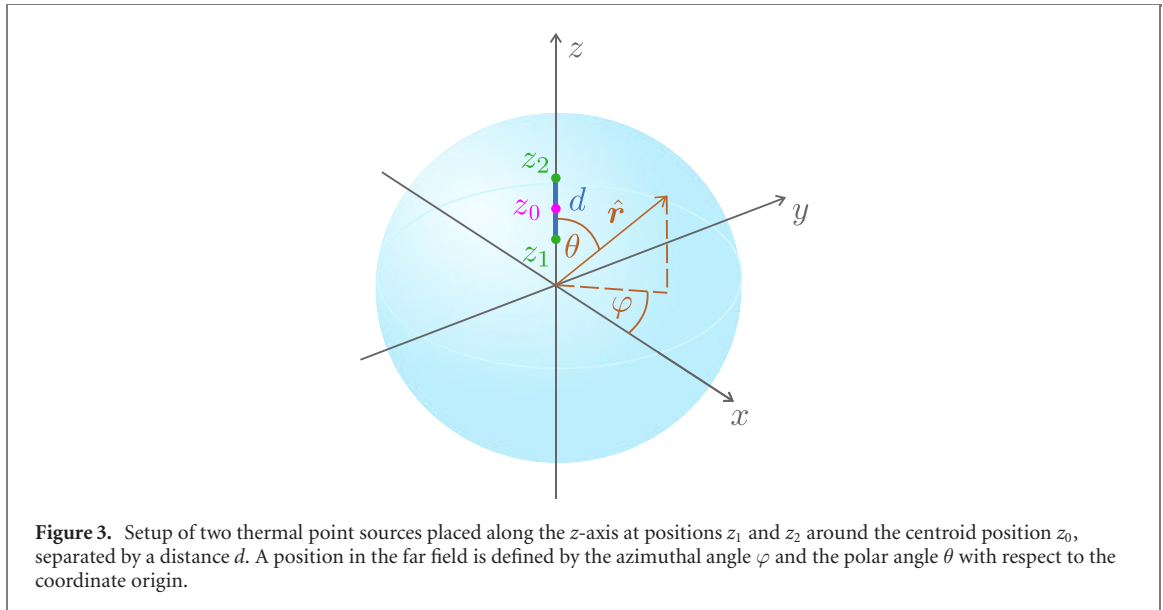
Figure 3. Setup of two thermal point sources placed along the z-axis at positions z_1 and z_2 around the centroid position z_0, separated by a distance d. A position in the far field is defined by the azimuthal angle φ and the polar angle θ with respect to the coordinate origin.

centroid z_0, the separation d and the relative strength q can be calculated as [51]

$$F_Q = 4 \begin{pmatrix} p^2 + 4q(1-q)\wp^2 & \left(q - \dfrac{1}{2}\right)p^2 & -iw\wp \\[2mm] \left(q - \dfrac{1}{2}\right)p^2 & \dfrac{1}{4}p^2 & 0 \\[2mm] -iw\wp & 0 & \dfrac{1 - w^2}{4q(1-q)} \end{pmatrix}. \tag{15}$$

Here, the different quantities entering the QFIM are

$$w = \langle\psi|\exp(idP)|\psi\rangle = \eta(d) = \exp\left(-\frac{d^2}{8x_R^2}\right),$$

$$p^2 = \langle\psi|P^2|\psi\rangle = \frac{1}{4x_R^2}, \tag{16}$$

$$\wp = \langle\psi|\exp(idP)P|\psi\rangle = \frac{id}{4x_R^2}\exp\left(-\frac{d^2}{8x_R^2}\right),$$

where $|\psi\rangle = \int dz\psi(z)|z\rangle$, $P = -i\partial_z$, and the analytical values were calculated using the Gaussian PSF of equation (37). One can see that in case of $q \neq \frac{1}{2}$, i.e., sources of different strength, all three parameters z_0, d and q become intertwined, such that it is a non-trivial task to estimate either of the three parameters.

However, the precision in a particular parameter can be calculated by taking the inverse of the diagonal elements of the inverse QFIM. In this way, the precision about the separation of the sources d is found to be [51]

$$H_d = p^2 \mathscr{D}^2 \frac{\wp^2 + p^2(1 - w^2)}{\mathscr{D}^2\wp^2 + p^2(1 - w^2)}, \tag{17}$$

where $\mathscr{D}^2 \equiv 4q(1-q)$.

In the special case of equally bright sources ($q = \frac{1}{2}$), one finds from equation (17) that

$$H_d = p^2, \tag{18}$$

i.e., a constant with respect to the separation d of the sources. This is the famous result found by Tsang *et al* [44]. Intuitively, the outcome can be attributed to the amount of information extractable from the state when we analyse the spatial distribution in the appropriate basis.

By contrast, for $q \neq \frac{1}{2}$, the precision H_d is not a constant as a function of the separation d. Indeed, in the case of a Gaussian PSF, by substituting equation (16) into equation (17), H_d becomes

Figure 4. Maximal precision of the separation d of two thermal point sources given by H_d in equation (19) (blue solid line), and precision obtained via direct imaging (yellow dotted line, see appendix A) as a function of d. For the special case of equally bright sources ($q = \frac{1}{2}$), the maximal precision remains constant, whereas direct imaging is not capable of achieving this precision in the limit $d \to 0$. However, for unequally bright sources ($q \neq \frac{1}{2}$) the 'Rayleigh curse' is unavoidable, meaning that even the maximal precision H_d drops off to zero for $d \to 0$, although it remains always higher than the precision obtained via direct imaging.

$$H_d = \frac{k^2 \mathrm{NA}^2 (1-q)q \left[\frac{1}{4}d^2 k^2 \mathrm{NA}^2 - \exp\left(\frac{1}{4}d^2 k^2 \mathrm{NA}^2\right) + 1 \right]}{d^2 k^2 \mathrm{NA}^2 (1-q)q - \exp\left(\frac{1}{4}d^2 k^2 \mathrm{NA}^2\right) + 1}, \tag{19}$$

where we have explicitly substituted $x_{\mathrm{R}} = 1/k\mathrm{NA}$ to highlight the dependence on the numerical aperture NA. For large separations $d \gg x_{\mathrm{R}} = 1/k\mathrm{NA}$, i.e., $dk\mathrm{NA} \gg 1$, the exponentials in the denominator and the numerator dominate and cancel each other, such that

$$H_d \approx k^2 \mathrm{NA}^2 (1-q)q = \text{constant}. \tag{20}$$

In the case of the other extreme, i.e., $d \to 0$, we can expand equation (19) in a Taylor series, which gives to lowest order

$$H_d \approx \frac{k^4 \mathrm{NA}^4 (1-q)q}{8(1-2q)^2} d^2. \tag{21}$$

In this limit, the precision drops to zero quadratically in d. In between these limiting cases we can identify the point at which H_d is reduced by 3 dB:

$$d \simeq \frac{2\sqrt{2 - 8q + 8q^2}}{k\mathrm{NA}} = 2\sqrt{2 - 8q + 8q^2}\, x_{\mathrm{R}}, \tag{22}$$

which is approximately $2.26 x_{\mathrm{R}}$ for $q = 0.1$. Thus, the numerical aperture crucially determines the starting point of the drop-off, i.e., for larger numerical apertures the drop-off starts only at smaller separations d. This feature is the essential aspect in the comparison of amplitude versus intensity interferometry accomplished in section 5.

In figure 4 we show the precision in equation (19) for $q = \frac{1}{2}$ and $q \neq \frac{1}{2}$, together with the precision obtained via the non-optimal measurement of direct imaging (see appendix A). As can be seen in figure 4, the precision achievable by direct imaging remains always smaller than the one obtained via optimal imaging, the former only approaching the optimal precision for $d \gg x_{\mathrm{R}}$. Further, for $q = \frac{1}{2}$, the maximal precision is a constant with respect to the separation of the two sources (see equation (18)), whereas for $q \neq \frac{1}{2}$ the 'Rayleigh curse' is unavoidable, even for the optimal case.

In this section we have given a broad outline for how to use the QFI in imaging situations, and applied the theory to the estimation of the separation between two distant thermal point sources. The quantum CRB places a limit on the precision with which such a parameter can be measured, but the bound does not immediately tell us how this precision can be achieved. For that we need to either calculate the symmetric logarithmic derivative operator L_d, or show that a given measurement saturates the quantum CRB. This will be the subject of the next two sections.
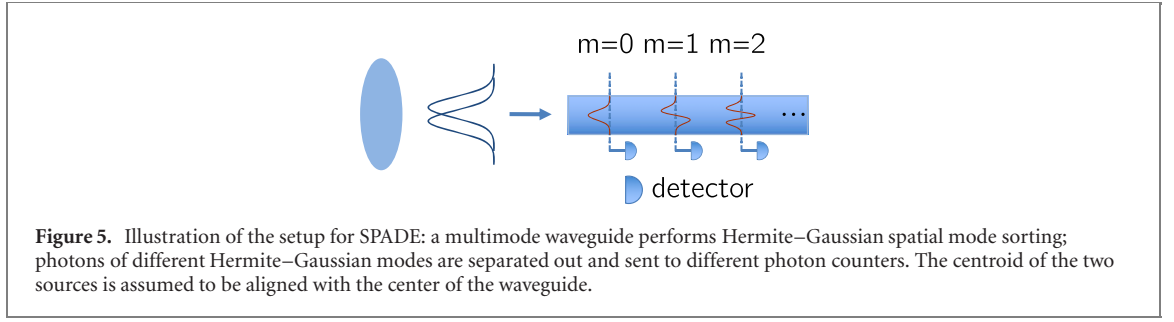
Figure 5. Illustration of the setup for SPADE: a multimode waveguide performs Hermite–Gaussian spatial mode sorting; photons of different Hermite–Gaussian modes are separated out and sent to different photon counters. The centroid of the two sources is assumed to be aligned with the center of the waveguide.

3. Amplitude interferometry

Next, we consider astronomical imaging methods that rely on amplitude interferometry, i.e., measuring the $G^{(1)}$ correlation function in the far field. In other words, these are phase-sensitive measurements. We have already considered direct (Galilean) imaging using traditional phase interferometry by means of lenses and telescopes like the ELT in section 2.1 (see also appendix A). For a one-dimensional problem, the PSF of a single point source is proportional to $\text{sinc}^2 x$ which can be approximated by the Gaussian function given in equation (37). In that case, we showed the FI for the separation d between two thermal point sources for two different values of the relative brightness q in figure 4. In the next two sub-sections, we consider the method employed by Nair *et al*, called SPADE, providing an optimal measurement of the separation d between two thermal point sources (section 3.1), and investigate two-mode interferometry that may be easier to implement, yet achieves the same resolution as SPADE (section 3.2).

3.1. Optimal amplitude interferometry—SPADE

Assuming that the PSF is Gaussian, we can devise an optimal measurement for estimating the angular separation between two sources. Rather than measuring the distribution of the photons on a screen, we decompose the light into Hermite–Gaussian spatial modes. To achieve this, our imaging system is assumed to consist of a multi-mode wave guide aligned such that the centroid of the two sources lies on the central axis of the wave guide. The signal is then demultiplexed so that photons of different Hermite–Gaussian modes in the wave guide are sent to different detectors (see figure 5). The Hermite–Gaussian spatial modes can be formally denoted by the basis states $\{|\Pi_m\rangle;\ m = 0, 1, 2, \ldots\}$, with

$$|\Pi_m\rangle = \int_{-\infty}^{\infty} \mathrm{d}z \Pi_m(z)|z\rangle, \quad m = 0, 1, 2, \ldots$$

$$\Pi_m(z) = \left(\frac{1}{2\pi x_\mathrm{R}^2}\right)^{\frac{1}{4}} \frac{1}{\sqrt{2^m m!}} H_m\left(\frac{z}{\sqrt{2}x_\mathrm{R}}\right) \exp\left(-\frac{z^2}{4x_\mathrm{R}^2}\right), \tag{23}$$

where H_m is the Hermite polynomial of order m, and z is the transverse position in the imaging plane [52]. The mode profiles for the first four modes are shown in figure 6. The probability that the photon is measured in mode m is given by the Born rule $\mathrm{Tr}(\rho|\Pi_m\rangle\langle\Pi_m|)$, where ρ is the state of light in the wave guide.

Next, we calculate the FI achieved by SPADE for equally bright sources and show that it is equal to the QFI. For a Gaussian PSF the probability that a photon is detected in a particular mode H_m is [44]
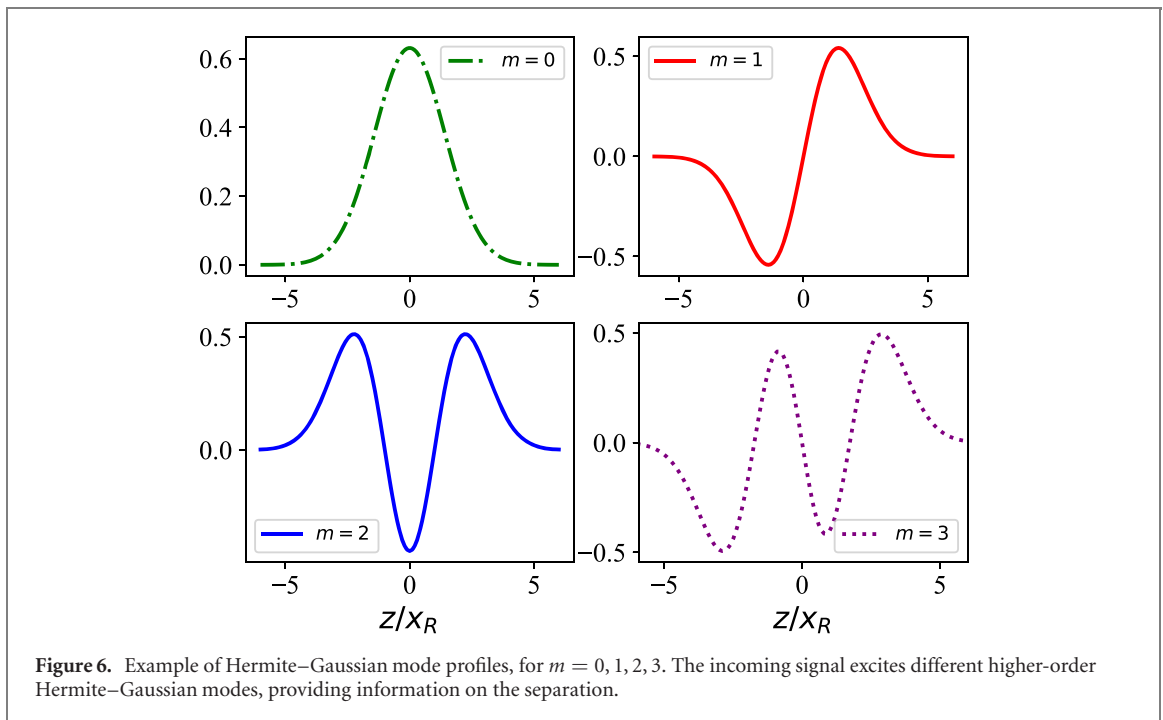
$$p(m) = \exp(-Q)\frac{Q^m}{m!}, \tag{24}$$

with

$$Q \equiv \frac{\zeta^2}{16x_\mathrm{R}^2}, \tag{25}$$

where we assume that the two distant point sources produce PSFs in the imaging plane centered at $z = \pm\zeta/2$, i.e., ζ is the separation of the sources on the image screen. Using equation (4), the FI for the parameter ζ is calculated as

$$F(\zeta) \approx N_s \sum_{m=0}^{\infty} p(m)\left[\frac{\partial}{\partial\zeta}\ln p(m)\right]^2 \approx \frac{N_s}{4x_\mathrm{R}^2}, \tag{26}$$

where N_s is the mean photon number of the sources. This is the classical FI achieved by SPADE. Note that in the limit $N_s \ll 1$ and for $q = \frac{1}{2}$, it follows from equation (19) that the QFI is also equal to $N_s/(4x_\mathrm{R}^2)$.

Figure 6. Example of Hermite–Gaussian mode profiles, for $m = 0, 1, 2, 3$. The incoming signal excites different higher-order Hermite–Gaussian modes, providing information on the separation.

Hence, the FI of SPADE achieves the theoretical maximum given by the QFI, i.e., SPADE corresponds to an optimal measurement of the separation between the two sources.

Intuitively, SPADE works for the following reason: given that the two distant point sources produce PSFs in the imaging plane centered at $z = \pm\zeta/2$, the wave function for small ζ can be approximated by

$$\psi\left(z \pm \frac{\zeta}{2}\right) \approx \psi(z) \pm \frac{\zeta}{2}\frac{\partial\psi(z)}{\partial z}. \qquad (27)$$

The function $\psi(z)$ is proportional to the $m = 0$ Hermite–Gaussian mode, while $\partial\psi(z)/\partial z$ is proportional to the $m = 1$ Hermite–Gaussian mode. Since these are orthogonal, they can be distinguished. The fundamental $m = 0$ spatial mode is insensitive to the parameter ζ. The $m = 1$ mode, however, *does* contain information about ζ, since $\Pi_1(z)$ is proportional to $\partial\psi(z)/\partial z$. The relative probabilities $p(m)$ for finding photons in the different Hermite–Gaussian modes provide the optimal estimator for ζ, which can be related directly to the angular separation $\theta = d/r$, the parameter of interest. Here, d is the distance between the sources, and r is the distance from the centroid to the imaging system.
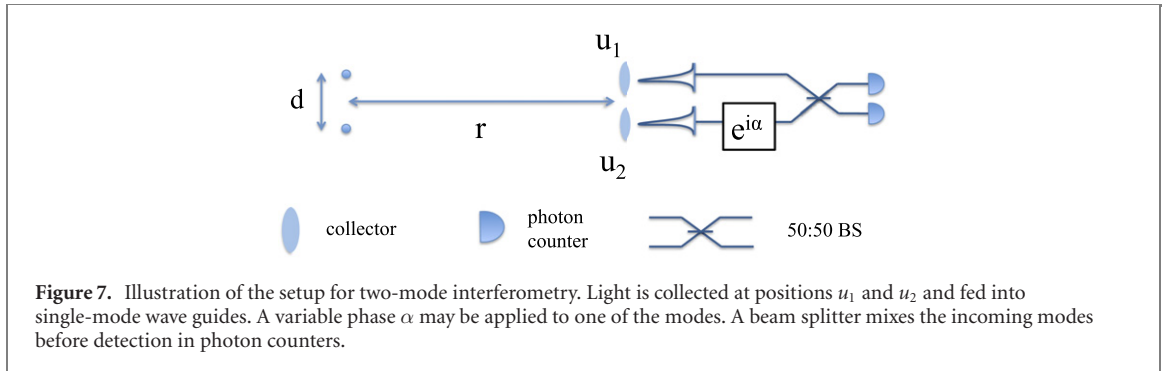
SPADE can be compared to that of a nulling interference coronagraph [53], where a phase-sensitive measurement is used in the analysis and also spatial mode-matching of the PSF is employed. In direct imaging, the fundamental mode contains very little information on the two sources and contributes a background to the spatial intensity measured, increasing the variance of the photon counts at each pixel (shot-noise). By using Hermite–Gaussian modes, the fundamental mode effectively filters out this background, thus substantially improving the signal-to-noise ratio. This method is similar to a nulling interference coronagraph that filters out the background of a much brighter stellar source so that an experimenter can extract information about nearby sources that may be much weaker.

Implementing SPADE is difficult, as different spatial modes need to be separated into different channels before detection. Several physical devices has been proposed [54], and a series of experiments [55–63] has confirmed the feasibility of SPADE-type measurements. The most accessible implementation remains an open question.

3.2. Optimal two-mode interferometry

SPADE effectively uses only the lowest two Hermite–Gaussian modes $m = 0$ and $m = 1$. This suggests that more generic two-mode interferometry may also provide optimal measurements of the source separation. The advantage is that two-mode interferometry is a mature technology. In this section we discuss the relative merits of two-mode interferometry for quantum imaging.

Let us consider two light-collecting fibers (collectors) that are separated by a distance $|u_1 - u_2|$. Assuming two equally bright incoherent point sources separated by a distance d, the QFI for the angular

Figure 7. Illustration of the setup for two-mode interferometry. Light is collected at positions u_1 and u_2 and fed into single-mode wave guides. A variable phase α may be applied to one of the modes. A beam splitter mixes the incoming modes before detection in photon counters.

separation θ can be calculated as [9]

$$F_Q(\theta) = \frac{k^2}{4}(u_1 - u_2)^2. \tag{28}$$

This expression is independent of θ, i.e., the separation d of the point sources, and therefore the measurement of the separation is in principle not limited by diffraction. A simple experimental scheme that can achieve this precision is shown in figure 7.

In what follows, we calculate the FI for the setup of figure 7 and show as before that its classical FI is identical to the QFI of equation (28). Therefore, like SPADE, the setup in figure 7 is an optimal measurement of the source separation.

We can write the state of a single photon originating from the two sources as

$$\rho \approx \frac{1}{2}|\psi_1\rangle\langle\psi_1| + \frac{1}{2}|\psi_2\rangle\langle\psi_2|. \tag{29}$$

Equation (29) corresponds to an incoherent mixture of the photon originating from source 1 (denoted by $|\psi_1\rangle$) and source 2 (denoted by $|\psi_2\rangle$). As the photons propagate towards the collectors at u_1 and u_2, the single photon states evolve to a very good approximation into (see figure 7)

$$|\psi_1\rangle \approx \frac{1}{\sqrt{2}}\left(|\psi_{u_1}\rangle + e^{i\phi+\alpha}|\psi_{u_2}\rangle\right),$$

$$|\psi_2\rangle \approx \frac{1}{\sqrt{2}}\left(|\psi_{u_1}\rangle + e^{-i\phi+\alpha}|\psi_{u_2}\rangle\right), \tag{30}$$

where $|\psi_{u_1}\rangle$ is the state of a photon collected in u_1, $|\psi_{u_2}\rangle$ is the state of a photon collected in u_2, and the phase ϕ is given by

$$\phi \approx \frac{1}{2}(u_1 - u_2)k\theta, \tag{31}$$

to an excellent approximation. Setting the adjustable phase $\alpha = 0$, the collected light is interfered at a 50:50 beam splitter, and the probabilities of finding the photon in detector 1 and detector 2, respectively, are given by

$$p_1 = \frac{1}{2}(1 + \cos\phi) \quad \text{and} \quad p_2 = \frac{1}{2}(1 - \cos\phi). \tag{32}$$

Substituting these probabilities into the expression for the FI in equation (4) yields

$$F(\theta) = \sum_{i=1,2} p_i \left[\frac{\partial}{\partial\theta}\ln p_i\right]^2 = \frac{k^2}{4}(u_1 - u_2)^2, \tag{33}$$

which is independent of θ and coincides with the QFI in equation (28). We note that for two-mode interferometry a similar phenomenon occurs as with SPADE, i.e., equal brightness of the two sources leads to a constant QFI, whereas unequal brightness gives rise to a drop-off of the QFI as the separation between the sources approaches zero [9].

The two-mode interferometric scheme has essentially the same resolution as SPADE. However, it removes the need for building a large system of lenses and mirrors for the telescope, as well as the experimental complexity for the SPADE measurement. Yet, the former comes at the cost of a reduced photon count rate by a factor of the ratio of the collecting areas. Also, in order to extract the angular separation from the measurements, the entire interferometer needs to be phase-stabilised to the same accuracy as any other $G^{(1)}$ measurement, i.e., to a fraction of a wavelength for the duration of the measurement. In astronomy, such optimal quantum telescopes have been implemented, e.g., in the GRAVITY interferometer as well as in CHARA.

4. Intensity interferometry

Next, we investigate the precision obtained via $G^{(2)}$ intensity interferometry, which requires correlating photons recorded at two detectors. Since the numerical aperture is defined by the distance between the two detectors, e.g., two telescopes, and since the correlations are generated only electronically, sometimes even only via post-processing, this setup allows for substantially larger numerical apertures than those achievable with the $G^{(1)}$ methods discussed in the previous section. Moreover, the telescopes can be simple in design as the photons have to be recorded only within their coherence time (or several coherence times, depending on the time resolution of the detectors), given, e.g., by the bandpass of the filter used in the setup. This is in contrast to amplitude interferometry where a phase-sensitive measurement of the electromagnetic field is needed, more likely to be affected by small perturbations, e.g., optical imperfections of the detectors or turbulences in the atmosphere. Eliminating such perturbations requires an elaborate design of the telescopes such as adaptive or active optics, limiting the numerical aperture of amplitude interferometry to typically < 500 m. Intensity interferometry on the other hand is not disturbed by detector imperfections or atmospheric turbulences. Moreover, the signal only depends on the source separation d and the relative strength q of the sources, but is insensitive to the centroid position z_0 of the light sources. In total, intensity correlation measurements appear simpler to implement while providing larger numerical apertures at potentially lower costs. The question is whether these advantages can overcome the reduced signal strength related to the small degeneracy parameter δ.

In what follows we investigate the precision of $G^{(2)}$ intensity correlation measurements using a lower bound on the FI. Considering realistic numerical apertures and photon fluxes, we will see that $G^{(2)}$ measurements indeed scale favorably in certain regions of the angular separation of the sources, in particular at very small separations, even with respect to the QFI of optimal $G^{(1)}$ measurements.

In general, for the state given in equation (41), consisting of an infinite sum over different photon numbers, the calculation of the FI for a particular measurement is challenging. We will thus compute only a general lower bound on the FI to estimate an unknown parameter array and compare it to the various $G^{(1)}$ methods discussed in the former section. However, for a fair comparison, we will consider different numerical apertures for $G^{(2)}$ and $G^{(1)}$ interferometry, i.e., we will allow for the reasons described above for the $G^{(2)}$ measurements much larger numerical apertures than for the $G^{(1)}$ measurements.

The intensity correlation function $G^{(2)}(\mathbf{r}_1, \mathbf{r}_2)$ at positions $\mathbf{r}_1$ and $\mathbf{r}_2$ is defined as

$$
\begin{aligned}
G^{(2)}(\mathbf{r}_1, \mathbf{r}_2) &= \langle E^\dagger(\mathbf{r}_1) E^\dagger(\mathbf{r}_2) E(\mathbf{r}_2) E(\mathbf{r}_1) \rangle \\
&= \langle I(\mathbf{r}_2) I(\mathbf{r}_1) \rangle - \delta(\mathbf{r}_1 - \mathbf{r}_2) \langle I(\mathbf{r}_1) \rangle,
\end{aligned}
\tag{34}
$$

where $E^\dagger(\mathbf{r})$ and $E(\mathbf{r})$ are the negative and positive frequency parts of the electric field operator at position $\mathbf{r}$. Since the operators $E^\dagger(\mathbf{r})$ and $E(\mathbf{r})$ do not commute, an extra term appears in equation (34) for the case that $\mathbf{r}_1 = \mathbf{r}_2$.

We suppose the detectors used for the $G^{(2)}$ measurements to have an area of $A = 10$ m $\times$ 10 m. This is a reasonable size taking into account that the telescopes are only photon collecting detectors which neither need adaptive nor active optics. The numerical aperture spanned by one detector is approximately $\sqrt{A}/r$, with r the distance from the stellar sources to the detector on Earth. However, the numerical aperture of the entire $G^{(2)}$ interferometer is given by the distance between the outermost detectors. In order to exploit multiple correlations at different detector separations, we will consider an ensemble of altogether 100 detectors, located at D different positions. This number of telescopes equals the number of detectors used for the system presently predominantly investigated for an implementation of $G^{(2)}$ intensity interferometry in astronomy, the Cherenkov Telescope Array (CTA) [64–66]. The sizes of the telescopes used in CTA (between 4 m and 23 m in diameter) span a similar range as assumed in our calculation and cover approximately the same total area.

Let $\mathcal{M}_1, \mathcal{M}_2 \subset \{1, \ldots, D\}$ denote two subsets of detector positions. We define the $G^{(2)}$ observation vector specified by $\mathcal{M}_1, \mathcal{M}_2$ as

$$
\mathbf{G}^{(2)}_{\mathcal{M}_1, \mathcal{M}_2} = \left(I^{(2)}_{i,j} \Big|_{i \in \mathcal{M}_1, j \in \mathcal{M}_2, i < j} \right)^\top,
\tag{35}
$$

where $I^{(2)}_{i,j}$ denotes the intensity correlation of detectors i and j. For the explicit calculation of the lower bounds for the general observation vector (35) we refer the reader to appendix C. Here, we assume $D = 1000$ available detector positions spanning a total length of 10 km. This is the maximum number of distinct positions given the size $A = 10$ m $\times$ 10 m of an individual telescope.
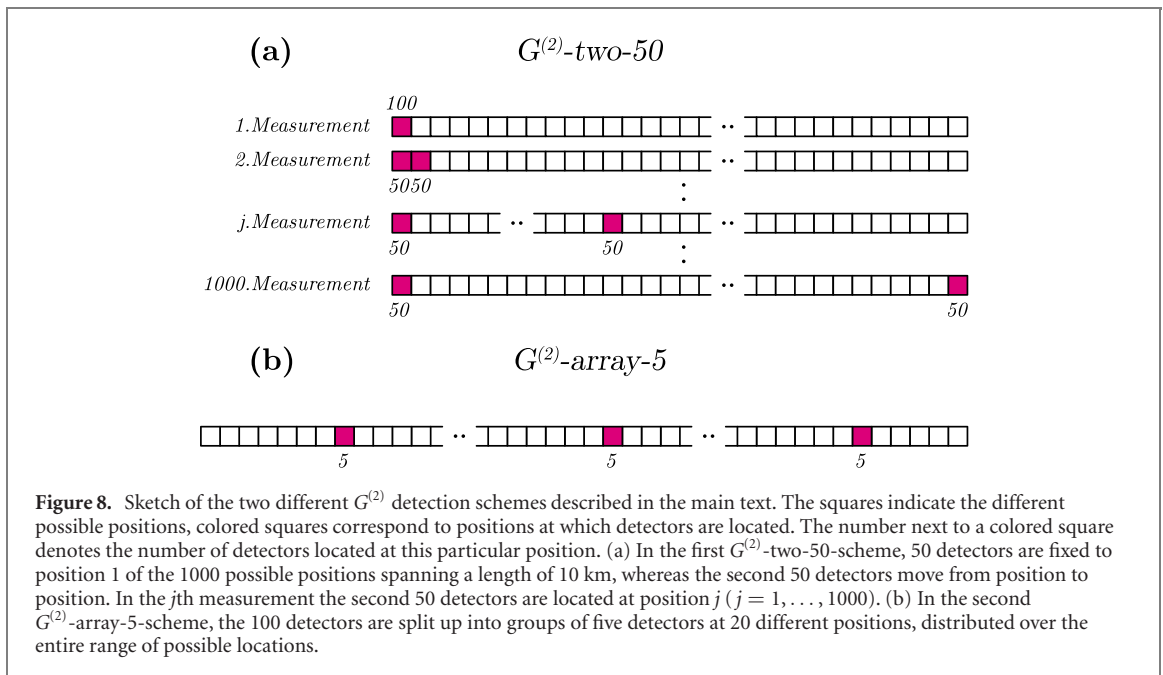
Figure 8. Sketch of the two different $G^{(2)}$ detection schemes described in the main text. The squares indicate the different possible positions, colored squares correspond to positions at which detectors are located. The number next to a colored square denotes the number of detectors located at this particular position. (a) In the first $G^{(2)}$-two-50-scheme, 50 detectors are fixed to position 1 of the 1000 possible positions spanning a length of 10 km, whereas the second 50 detectors move from position to position. In the jth measurement the second 50 detectors are located at position j ($j = 1, \ldots, 1000$). (b) In the second $G^{(2)}$-array-5-scheme, the 100 detectors are split up into groups of five detectors at 20 different positions, distributed over the entire range of possible locations.

In the following, we describe two different measurement schemes each utilizing the 100 detectors. In the first scheme, called $G^{(2)}$-two-50-scheme, we suppose that we fix 50 detectors to the position $i = 1$ ($\mathcal{M}_1 = \{1\}$), and the remaining 50 detectors move from measurement to measurement to the positions $j = 1$ to $j = 1000$ (see figure 8(a)). In this case, for the jth measurement, the $G^{(2)}$ observation vector consists of only one element reading $G^{(2)}_{\mathcal{M}_1, \mathcal{M}_2} = I^{(2)}_{1,j}$. We further assume that the measurements are independent of each other so that we can add the FI as well as the lower bounds of the individual measurements. In the end, we divide the lower bound by the number of measurements to get an average precision per measurement.

The second scheme, which we call $G^{(2)}$-array-5-scheme, involves multiple positions within the array. Here, we assume that the 100 detectors are placed at 20 different positions, i.e., five detectors at each position in the array (see figure 8(b)). We denote the corresponding locations as $L_1, L_2, \ldots, L_{20} \in \{1, \ldots, D\}$. In figure 8(b), for instance, these locations are $L_1 = 8, \ldots, L_{20} = 995$. Considering all possible two-point correlations of the 20 positions $L_1, L_2, \ldots, L_{20}$ contained in the array, i.e., $\mathcal{M}_1 = \mathcal{M}_2 = \{L_1, L_2, \ldots, L_{20}\}$, the observation vector reads
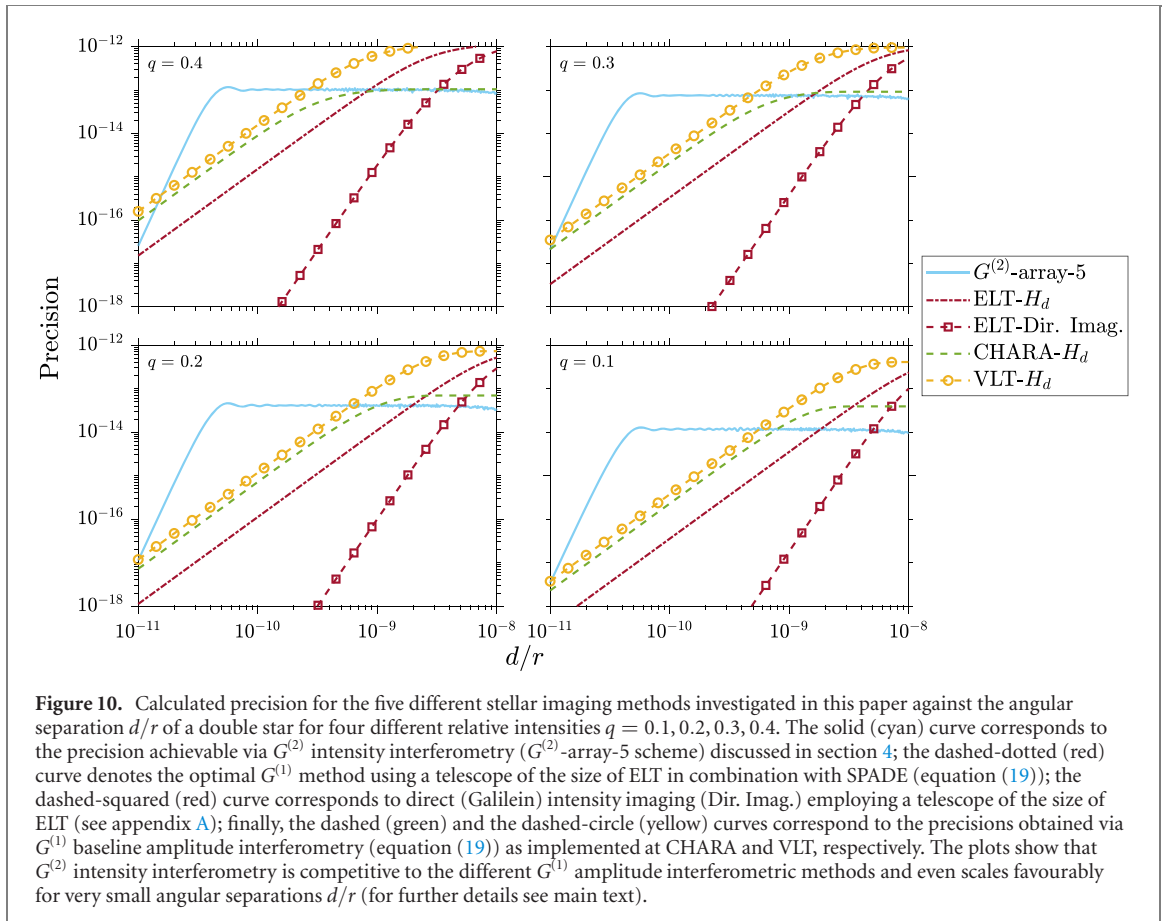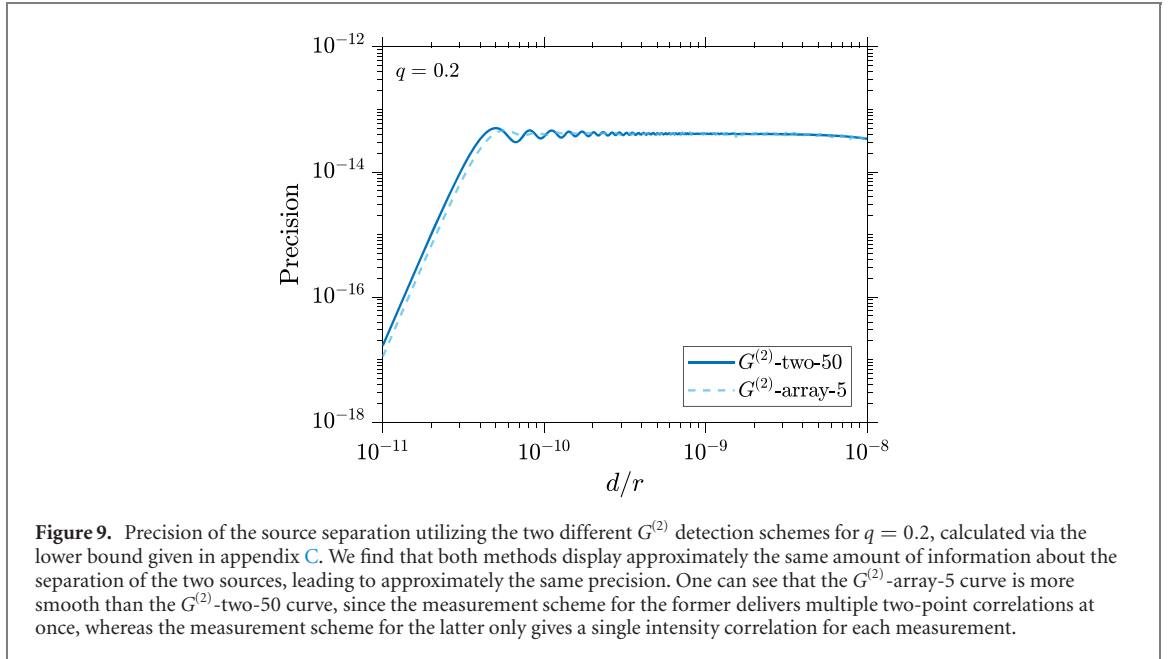
$$\mathbf{G}^{(2)}_{\text{Array}} = \left(I^{(2)}_{L_1,L_1}, I^{(2)}_{L_1,L_2}, \ldots, I^{(2)}_{L_{20},L_{20}} \right)^{\top}. \tag{36}$$

In this case, we divide the 1000 detector positions in intervals of $1000/20 = 50$ positions, whereby in each interval one detector position is populated with five detectors. We average the lower bound over five realizations, where for each realization the populated detector position of each interval is randomly chosen.

In figure 9 we show for $q = 0.2$ for both $G^{(2)}$ detection schemes the calculated lower bound of the FI matrix entry corresponding to the separation, directly related to the precision in estimating the separation of the two sources. We find that both $G^{(2)}$ measurement schemes achieve approximately the same precision. However, since the $G^{(2)}$-array-5 scheme provides multiple two-point correlations at once, the curve is more smooth compared to the $G^{(2)}$-two-50 scheme, which only provides a single two-point correlation for each shot giving rise to small oscillations.

5. Comparison of $G^{(1)}$ and $G^{(2)}$ methods

In this section, we compare $G^{(2)}$ intensity interferometry as discussed in section 4 with the various methods for $G^{(1)}$ amplitude interferometry considered in section 3. For the comparison we use the four different relative source strengths $q = 0.1, 0.2, 0.3, 0.4$. In figure 10 we display the results obtained for the $G^{(2)}$-array-5 scheme, i.e., using an array of 100 detectors distributed at 20 different positions with a possible maximum baseline of 10 km, and the outcomes of the four different interferometric methods discussed in section 3. The latter are: traditional $G^{(1)}$ amplitude interferometry using a single telescope with mirror size 39.3 m as realized at the ELT; optimal $G^{(1)}$ amplitude interferometry using the same ELT-sized telescope in combination with SPADE; $G^{(1)}$ baseline amplitude interferometry using an array of telescopes the size

Figure 9. Precision of the source separation utilizing the two different $G^{(2)}$ detection schemes for $q = 0.2$, calculated via the lower bound given in appendix C. We find that both methods display approximately the same amount of information about the separation of the two sources, leading to approximately the same precision. One can see that the $G^{(2)}$-array-5 curve is more smooth than the $G^{(2)}$-two-50 curve, since the measurement scheme for the former delivers multiple two-point correlations at once, whereas the measurement scheme for the latter only gives a single intensity correlation for each measurement.

Figure 10. Calculated precision for the five different stellar imaging methods investigated in this paper against the angular separation d/r of a double star for four different relative intensities $q = 0.1, 0.2, 0.3, 0.4$. The solid (cyan) curve corresponds to the precision achievable via $G^{(2)}$ intensity interferometry ($G^{(2)}$-array-5 scheme) discussed in section 4; the dashed-dotted (red) curve denotes the optimal $G^{(1)}$ method using a telescope of the size of ELT in combination with SPADE (equation (19)); the dashed-squared (red) curve corresponds to direct (Galilein) intensity imaging (Dir. Imag.) employing a telescope of the size of ELT (see appendix A); finally, the dashed (green) and the dashed-circle (yellow) curves correspond to the precisions obtained via $G^{(1)}$ baseline amplitude interferometry (equation (19)) as implemented at CHARA and VLT, respectively. The plots show that $G^{(2)}$ intensity interferometry is competitive to the different $G^{(1)}$ amplitude interferometric methods and even scales favourably for very small angular separations d/r (for further details see main text).

8.2 m with a maximum baseline of 130.2 m as realized at the VLT; $G^{(1)}$ baseline amplitude interferometry using an array of telescopes the size 1 m with a maximum baseline of 330 m as in CHARA. For all interferometric methods we assume a photon flux from the double star system of 2×10^{-2} photons per coherence time within an area of 10 km × 10 km at a wavelength of 600 nm; for equally bright sources ($q = \frac{1}{2}$), this would mean that each source emits on average 10^{-2} photons per mode. The telescope sizes, corresponding average photon numbers per telescope, baselines, corresponding numerical apertures, and numbers of telescopes considered for each interferometer/telescope in figure 10 are listed in table 1.

Table 1. Comparison of the different telescope sizes, average photon numbers per telescope, baselines, corresponding numerical apertures, and numbers of telescopes used for the numerical calculations displayed in figure 10.

Method	Diameter$_{tel}$	$N_{s,tel}$	Baseline	NA	#tel
$G^{(2)}$	10 m	2×10^{-8}	10 km	10^{-8}	100
ELT	39.3 m	3.1×10^{-7}	—	3.9×10^{-11}	1
CHARA	1 m	2×10^{-10}	330 m	3.3×10^{-10}	2
VLT	8.2 m	1.3×10^{-8}	130.2 m	1.3×10^{-10}	2

Note that for the numerical simulations in figure 10 we used a small (relative to astronomical) distance r ($= 10^{12}$ m, $\approx 10^{-4}$ light years) to the two sources (and as such unrealistic large numerical apertures) to avoid complications with very small numbers in the calculations; however we take the distance large enough to be still in the far field regime. Note that this does not change the relative position of the curves in figure 10. In the figure, the precision for direct imaging using the ELT telescope is calculated via the procedure explained in appendix A for the corresponding PSF, and the precision of the $G^{(2)}$ method is calculated via the lower bound given in appendix C.

From figure 10 we can see that for the parameters of table 1, $G^{(2)}$ intensity interferometry is indeed competitive to $G^{(1)}$ amplitude interferometry. This is surprising, since $G^{(2)}$ measurements require two photons to be measured coincidentally, whereas $G^{(1)}$ measurements only need single photon detection; the precision of $G^{(2)}$ intensity interferometry depends thus quadratically on the average photon number per mode, i.e., the degeneracy parameter δ, whereas for $G^{(1)}$ amplitude interferometry the precision scales linearly with δ. However, in both cases the precision also scales quadratically with the numerical aperture (see also the discussion in section 2.2 following equation (19)). As in $G^{(2)}$ intensity interferometry the numerical aperture can exceed the numerical aperture of $G^{(1)}$ methods by a factor of 100 or larger, this can indeed compensate for the lower number of two-photon coincident detection events. In particular, as shown in figure 10, when considering very small stellar separations (or feature sizes), we find a regime of angular separations d/r for which the precision of the $G^{(2)}$ method clearly outperforms the one of the $G^{(1)}$ methods. Here, the advantage of the much larger numerical apertures achievable in $G^{(2)}$ intensity interferometry compared to $G^{(1)}$ amplitude interferometry clearly overcomes the drawback of the quadratic dependency on the small degeneracy parameter δ at optical frequencies. Yet, the slope of the $G^{(2)}$ precision drop-off is steeper than the one of the $G^{(1)}$ precision as the latter depends only linearly on δ.

6. Possible implementations of VLBII

Currently, in astronomical imaging, both amplitude interferometry and intensity interferometry are employed. Direct (Galilean) imaging is presently pushed to the limit with the ELT in Chile, having a compound mirror of 39.3 m in diameter [3]. Baseline amplitude interferometry is realized by GRAVITY at VLT and CHARA using baselines of 130.2 [67] and 330 m [5], respectively. Recently, intensity interferometry was implemented with four telescopes by the VERITAS collaboration at a maximum baseline of 172.5 m [30]; already beforehand, spatial intensity correlations have been measured with starlight using smaller baselines [27, 29]. While so far the baselines utilized in intensity interferometry have been of reasonable size, interesting prospects arise at baselines of the order of 2 km or even 10 km. Both will allow for sub-milli-arcsecond resolution. Presently, the CTA is studied for this purpose as a possible candidate for VLBII aiming for a baseline of 2.4 km [64, 65, 68].

Intensity interferometry on stars as faint as apparent magnitude five are estimated to be possible with $G^{(2)}$ setups using currently existing Cherenkov telescopes with diameters on the order of 4 m to 23 m [30]. The future CTA is projected to allow intensity interferometric observations of stars even as faint as apparent magnitude 7 [69]. At these apparent magnitudes around 2700 (magnitude 5) and 25 000 (magnitude 7) astronomical targets can be selected for observation [70], however not all of them will be observable from a given location on earth or emitting into the required optical bands. Only about 2600 objects from the bright star catalogue can be selected for VLBII observation when additionally including spectral limitations [68, 71]. Also implementing third-order intensity interferometry at CTA seems possible, and would aid the image reconstruction process [72].

At baselines of the order of 10 km, angular resolutions on the order of $\sim 5\,\mu$as are possible for $G^{(2)}$ setups at visible wavelengths. While such high angular resolutions are probably not required for diameter measurements of main sequence stars brighter than apparent magnitude 8 (having typical angular resolutions not far below ~ 0.1 mas [73]) they can be utilized for a number of other interesting astronomical measurements. Resolutions of ~ 0.05 mas are required to image dark or bright spots of stars

within the milky way [69], measure stellar deformities due to rotation [74], circumstellar disks and hot star winds [31], or properties of interacting binary stars [66]. Even higher angular resolutions are beneficial if stellar images should be reconstructed for small and faint stars. These ultra-high angular resolutions are also needed if exoplanet transits at distant stars are to be studied, with exoplanets typically having an angular extent 20 times smaller than the star [73]. Additionally, these high resolutions might facilitate the study of otherwise unresolved features in distant galaxies or distant supernovae.

Observations of pre-series stars in their formation and evolved stars up to planetary nebulae has been proposed for amplitude interferometry [73]. According to our estimations, this should be achievable with VLBII, yet utilizing presumably much simpler setups. This implies that nearly all stages in the life of a star would be observable with VLBII at higher resolutions than with amplitude interferometry considering realistic setups.

7. Conclusions

In conclusion, we have presented a quantitative comparison of the precision achievable in stellar astronomy, using $G^{(1)}$ amplitude interferometry on the one hand and $G^{(2)}$ intensity interferometry on the other hand for the benchmark problem of determining the separation between two adjacent stars. The comparison is based on well-established measures from estimation theory, the Fisher and the quantum Fisher information. The two quantities allow for the determination of the amount of information, i.e., the precision, that one can achieve in a given measurement (FI) or even in an optimal measurement (QFI) of the electromagnetic field for estimating the centroid z_0, the separation d and the relative strength q of a double star system. After a short introduction to the FI and the QFI in section 2, we investigated in section 3 various imaging methods which make use of $G^{(1)}$ amplitude interferometry. The latter included direct (Galilean) imaging as realized at the ELT in Chile, optimal imaging as could be implemented at the ELT by use of SPADE, and another optimal imaging method using baseline $G^{(1)}$ interferometry as implemented, e.g., in the GRAVITY Collaboration and at CHARA. In section 4, we determined the precision which one can achieve via $G^{(2)}$ measurements by use of very large baseline intensity interferometry (VLBII), employing real parameters as implemented, e.g., at the southern CTA in Chile.

In section 5, we compared the two methods and found that for realistic parameters VLBII can indeed be competitive and even outperform $G^{(1)}$ amplitude interferometry. The reason is that even though $G^{(2)}$ intensity interferometry scales quadratically with the small degeneracy parameter δ while $G^{(1)}$ amplitude interferometry scales linearly with δ, both methods depend quadratically on the numerical aperture. Since for VLBII the latter can be orders of magnitude larger compared to realistic $G^{(1)}$ systems, the precision in $G^{(2)}$-measurements can be of comparable value and even overcome the one of $G^{(1)}$ amplitude interferometry, in particular when considering very small stellar separations or feature sizes of the object of interest.

More precisely, calculating the QFIM and analyzing the corresponding analytic expression for the precision about the separation of the two stars, we learned that for optimal $G^{(1)}$ measurements the precision drops off to zero in the limit of infinitesimally small separations, depending on the numerical aperture. I.e., for larger numerical apertures the drop-off starts at smaller angular separations d/r (see the discussion following equation (19)). This statement holds true in a similar fashion for $G^{(2)}$ measurements (even though the detection involves two photons what steepens the slope of the drop-off). Figure 10 shows that the different onsets of these reductions lead to a regime of very small separations of the double star system for which the precision achievable with $G^{(2)}$ intensity interferometry is higher than that of $G^{(1)}$ amplitude interferometry.

In the future, both optimal $G^{(1)}$ amplitude interferometry and VLBII can be pushed to increase performance. For example, it is possible to use quantum entangled networks to further increase the numerical aperture in $G^{(1)}$ amplitude interferometry by teleporting collected photons over large distances [75–77]. Teleportation preserves the relative phase of the photons, and photon transmission losses can be side-stepped by prior established photonic entanglement. VLBII with decent baselines was recently established, but remain at the testing stage [27, 29, 30]. Larger arrays like CTA have been considered an ideal implementation of VLBII, with prospective baselines of about ∼2 km and joint recovery of many spatial frequencies, utilizing about 100 telescopes at once [65], which would enable the reconstruction of conventional images [69, 74]. VLBII results might be further improved by exploring optimal detector array geometries or exploiting higher-order spatial correlations [78]. Envisioning VLBII with 100 telescopes of diameter ∼10 m and baselines on the order of ∼10 km, resolutions of ∼ 0.005 mas are possible, surpassing the resolution of current and planned amplitude interferometers by a factor of 20 or more, and even surpassing the resolution of the EHT Collaboration.

Acknowledgments

Data availability statement

The data that support the findings of this study are available upon reasonable request from the authors.

Appendix A. Application of classical estimation theory to imaging two thermal point sources—direct imaging precision

As an example of how to apply estimation theory to imaging two thermal point sources, first recall that Rayleigh's criterion [79] establishes the minimum separation between two incoherent point sources required in order to resolve them. It arises from the diffraction of light through the finite aperture of an optical system, even as large as the ELT. As a consequence, a point-like source will have a finite extension on the image plane, known as the PSF [80, 81]. Two points that are closer together in the image plane than the width of the PSF will be difficult to resolve due to the substantial overlap of their images. The size of the PSF is of the order of the Rayleigh length $x_R = 1/k\text{NA}$, where k is the wave number and NA is the numerical aperture that characterizes the optical system.

For a Gaussian PSF with a width equal to the Rayleigh length, the image of a single point source at position z_0 (in the imaging plane) with unit intensity becomes

$$\psi(z - z_0) = \frac{1}{\sqrt[4]{2\pi x_R^2}} \exp\left[-\frac{(z-z_0)^2}{4x_R^2}\right]. \tag{37}$$

The corresponding normalised intensity profile is given by $|\psi(z-z_0)|^2$, which is equal to the probability distribution $p(z|z_0)$ of finding a photon at position z in the imaging plane given that the PSF is centered around z_0. Assuming now two thermal light sources at positions z_1 and z_2 the one-photon truncated state (neglecting the vacuum) can be written as

$$\rho = q|\psi_+\rangle\langle\psi_+| + (1-q)|\psi_-\rangle\langle\psi_-|, \tag{38}$$

where

$$|\psi_\pm\rangle = \int dz\, \psi_\pm(z)|z\rangle. \tag{39}$$

Here, q characterizes the relative source strength and z is the image plane coordinate. Assuming unit magnification $\psi_-(z) = \langle z - z_1|\psi\rangle = \psi(z - z_1)$ denotes the state of a photon originating from the source at z_1, $\psi_+(z) = \langle z - z_2|\psi\rangle = \psi(z - z_2)$ denotes the state of a photon originating from the source at z_2. The probability to detect a photon at position z is then given by

$$p(z) = \langle z|\rho|z\rangle = q|\psi_+(z)|^2 + (1-q)|\psi_-(z)|^2. \tag{40}$$

The multi-parameter FI matrix of equation (6) for direct imaging is then calculated with the Gaussian PSF of equation (37) and the probability distribution of equation (40) with respect to the three parameters, given by the centroid z_0, the separation d and the relative source strength q. By numerically calculating the inverse of the FI matrix and taking the inverse of the diagonal element corresponding to the separation we find the precision bound for direct imaging in terms of equation (8).

Appendix B. Quantum state of two thermal light sources

The two thermal points sources illustrated in figure 3 can be described by a pair of complex amplitudes $\mathbf{A} = (A_-, A_+)^\top$ with respective photon numbers $N_{s,1} = \mathbb{E}_A[|A_+|^2] = N_s q$ and $N_{s,2} = \mathbb{E}_A[|A_-|^2] = N_s(1 - q)$ [15], where N_s is the total average photon number and $q \in [0, 1]$ describes the relative strength of the sources. Here, $\mathbb{E}_A$ denotes the expectation value with respect to $\mathbf{A}$. The density

matrix of the light field produced by the two sources in the far field in the so-called Glauber–Sudarshan P-representation is [15]

$$\rho_d = \int_{\mathbb{C}^2} d^2 A_+ d^2 A_- \, P_{N_s}(\boldsymbol{A}) |\psi_{\boldsymbol{A},d}\rangle \langle \psi_{\boldsymbol{A},d}|, \tag{41}$$

where the joint probability distribution is given by the product of the individual probability distributions as

$$P_{N_s}(\boldsymbol{A}) = P_{N_{s,1}}(A_+) P_{N_{s,2}}(A_-) \tag{42}$$

with

$$P_{N_{s,1/2}}(A_\pm) = \left(\frac{1}{\pi N_{s,1/2}} \right) \exp\left(-\frac{|A_\pm|^2}{N_{s,1/2}} \right). \tag{43}$$

In equation (41), $|\psi_{\boldsymbol{A},d}\rangle$ represents a coherent state in the far field with mean number of photons N_s, which is an eigenstate of the positive frequency field operator $E(\mathbf{r})$

$$E(\mathbf{r})|\psi_{\boldsymbol{A},d}\rangle = \psi_{\boldsymbol{A},d}(\mathbf{r})|\psi_{\boldsymbol{A},d}\rangle, \tag{44}$$

with eigenvalue

$$\psi_{\boldsymbol{A},d}(\mathbf{r}) = A_+ \psi(\mathbf{r} - \boldsymbol{z}_2) + A_- \psi(\mathbf{r} - \boldsymbol{z}_1), \tag{45}$$

where $\boldsymbol{z}_{1,2} = \boldsymbol{z}_0 \mp \boldsymbol{d}/2$, $\boldsymbol{d} = (0,0,d)^\top$, and $\psi(\mathbf{r})$ denotes the photonic wave function in the far field.

An important quantity is the overlap between the wave functions for a given translation $\boldsymbol{a}$

$$\eta(\boldsymbol{a}) = \int d^2 r \, \psi^*(\mathbf{r}) \psi(\mathbf{r} - \boldsymbol{a}). \tag{46}$$

In general, $\eta(\boldsymbol{a})$ is non-zero, which means that the wave-functions coming from the two sources are non-orthogonal spatially, which is what makes estimation based on photon counting on a screen difficult.

Appendix C. Intensity interferometry precision

Consider a general vector random variable $\boldsymbol{X} = (X_1, \ldots, X_M)^\top \in \mathbb{R}^M$ whose probability density $p_{\boldsymbol{X}|\boldsymbol{\Theta}}(\boldsymbol{x}|\boldsymbol{\theta})$ depends on $\boldsymbol{\theta}$. The FI $\mathcal{F}(\boldsymbol{\theta})$ of $\boldsymbol{X}$ on $\boldsymbol{\theta}$ is bounded from below by [82]

$$\mathcal{F}(\boldsymbol{\theta}) \succeq \left(\frac{\partial \boldsymbol{\mu}}{\partial \boldsymbol{\theta}} \right)^\top \boldsymbol{C}^{-1} \left(\frac{\partial \boldsymbol{\mu}}{\partial \boldsymbol{\theta}} \right), \tag{47}$$

where $\boldsymbol{\mu} = (\langle X_1 \rangle(\boldsymbol{\theta}), \ldots, \langle X_M \rangle(\boldsymbol{\theta}))^\top$ is the mean observation vector of the random vector $\boldsymbol{X}$ and $\boldsymbol{C} = \langle (\boldsymbol{X} - \boldsymbol{\mu})(\boldsymbol{X} - \boldsymbol{\mu})^\top \rangle(\boldsymbol{\theta})$ is the covariance matrix of $\boldsymbol{X}$. In what follows, we specify the random vectors for second-order intensity correlation measurements and calculate the corresponding expectation values.

The correlation function $G^{(2)}(\mathbf{r}_1, \mathbf{r}_2)$ at positions $\mathbf{r}_1$ and $\mathbf{r}_2$ is defined as

$$\begin{aligned} G^{(2)}(\mathbf{r}_1, \mathbf{r}_2) &= \langle E^\dagger(\mathbf{r}_1) E^\dagger(\mathbf{r}_2) E(\mathbf{r}_2) E(\mathbf{r}_1) \rangle \\ &= \text{Tr}[E(\mathbf{r}_2) E(\mathbf{r}_1) \rho E^\dagger(\mathbf{r}_1) E^\dagger(\mathbf{r}_2)] \\ &= \mathbb{E}_{\boldsymbol{A}} \left[|\psi_{\boldsymbol{A},d}(\mathbf{r}_1)|^2 |\psi_{\boldsymbol{A},d}(\mathbf{r}_2)|^2 \right], \end{aligned} \tag{48}$$

where the optical equivalence theorem was used in the last line of equation (48). Here, $\mathbb{E}_{\boldsymbol{A}}[.]$ denotes the expectation value with respect to the source amplitudes. Since the light is collected by detectors, the positions $\mathbf{r}_1$ and $\mathbf{r}_2$ are replaced by two detector indices i and j with detector areas

$$\mathcal{A}_{i/j} = \{(\varphi, \theta) : -\tilde{\varphi} \leqslant \varphi < \tilde{\varphi}, l_{i/j} \leqslant \theta \leqslant r_{i/j}\}, \tag{49}$$

where $|r_{i/j} - l_{i/j}| = 2\tilde{\theta}/D$ and $\tilde{\theta}$ denotes the angle of the numerical aperture. Then the correlation function of a single shot becomes an intensity correlation $I_{i,j}^{(2)}$ of detectors i and j. Thus the random vectors for the second-order intensity correlation measurements are the ones specified in equation (35). We now evaluate the corresponding expectation values.

We assume that the photons are freely propagating, i.e., their wave function can be described as a spherical wave

$$\psi(\mathbf{r}) = \frac{1}{\sqrt{4\tilde{\varphi} \sin \tilde{\theta}}} \frac{e^{ikr}}{r}. \tag{50}$$

We then have for a displaced emission at point z the wave function

$$\psi(\mathbf{r} - \mathbf{z}) = \frac{1}{\sqrt{4\tilde{\varphi} \, \sin \tilde{\theta}}} \frac{e^{ik|\mathbf{r}-\mathbf{z}|}}{|\mathbf{r} - \mathbf{z}|}. \tag{51}$$

In the far field we can approximate $|\mathbf{r} - \mathbf{z}| \approx |\mathbf{r}| = r$ in the denominator. In the phase we need a more sensitive approximation as $|\mathbf{r} - \mathbf{z}| \approx r - \mathbf{rz}/r = r - z\cos\theta$. In what follows we neglect the $1/r$ dependence and the constant phase coming from the first term in $r - z\cos\theta$. Therefore, the states can be written in far-field approximation as

$$\psi(\mathbf{r} - \mathbf{z}_{1/2}) = \frac{1}{\sqrt{4\tilde{\varphi} \, \sin \tilde{\theta}}} e^{-ik(z_0 \mp d/2)\cos\theta}. \tag{52}$$

Now, considering the finite detector size equation (49) the mean values of the conditional intensity correlations $I^{(2)}_{i,j|A}$ yield

$$\mu_{i,j|A} = \int_{\mathcal{A}_i} d^2 r_1 \int_{\mathcal{A}_j} d^2 r_2 \, |\psi_{A,d}(\mathbf{r}_1)|^2 |\psi_{A,d}(\mathbf{r}_2)|^2 \tag{53}$$

$$= \eta_{i|A} \eta_{j|A}$$

with

$$\eta_{p|A} := \int_{\mathcal{A}_p} d^2 r \, |\psi_{A,d}(\mathbf{r})|^2 \tag{54}$$

$$= |A_+|^2 \alpha_p + |A_-|^2 \alpha_p + A_+^* A_- \beta_p + A_+ A_-^* \beta_p^*,$$

where

$$\alpha_p := \int_{\mathcal{A}_p} d^2 r |\psi(\mathbf{r} - \mathbf{z}_2)|^2 \tag{55}$$

$$= \frac{1}{2 \sin \tilde{\theta}} \left[\cos(l_p) - \cos(r_p) \right],$$

$$\beta_p := \int_{\mathcal{A}_p} d^2 r \, \psi^*(\mathbf{r} - \mathbf{z}_2) \psi(\mathbf{r} - \mathbf{z}_1)$$

$$= \frac{1}{2 \sin \tilde{\theta} ikd} \left[e^{ikd \, \cos(l_p)} - e^{ikd \, \cos(r_p)} \right]. \tag{56}$$

Using equation (48) and the following identities, fulfilled by the source amplitudes A_+ and A_-

$$\mathbb{E}_A[A_+^* A_-] = \mathbb{E}_A[A_-^* A_+] = 0, \tag{57}$$

$$\mathbb{E}_A[A_+ A_-] = \mathbb{E}_A[A_- A_+] = 0, \tag{58}$$

$$\mathbb{E}_A[|A_+|^2] = N_s q, \mathbb{E}_A[|A_-|^2] = N_s(1 - q) \tag{59}$$

the expectation values $\mu_{i,j} = \mathbb{E}_A[\mu_{i,j|A}]$ can be calculated, which can then be used to find the derivatives with respect to the unknown parameters. Analogously the elements of the covariance matrix can be calculated via

$$C_{i,j,k,l} = \mathbb{E}[I^{(2)}_{i,j} I^{(2)}_{k,l}] - \mu_{i,j}\mu_{k,l}. \tag{60}$$

We are then able to compute numerically the lower bound equation (47) for the different measurement schemes characterized in the main text.

ORCID iDs

Manuel Bojer ⓘ https://orcid.org/0000-0003-2897-8548
Sebastian Karl ⓘ https://orcid.org/0000-0001-9920-9215
Stefan Richter ⓘ https://orcid.org/0000-0002-2681-039X
Joachim von Zanthier ⓘ https://orcid.org/0000-0001-7013-0888

References

[1] Akiyama K *et al* 2019 First M87 event horizon telescope results: I. The shadow of the supermassive black hole *Astrophys. J. Lett.* **875** L1

[2] Lipson A, Lipson S G and Lipson H 2010 *Optical Physics* (Cambridge: Cambridge University Press)

[3] de Zeeuw T, Tamai R and Liske J 2014 Constructing the E-ELT *Messenger* **158** 3 https://www.eso.org/sci/publications/messenger/archive/no.158-dec14/messenger-no158-3-6.pdf

[4] GRAVITY Collaboration 2017 First light for GRAVITY: phase referencing optical interferometry for the very large telescope interferometer *Astron. Astrophys.* **602** A94

[5] Anugu N *et al* 2020 MIRC-x: a highly sensitive six-telescope interferometric imager at the CHARA array *Astron. J.* **160** 158

[6] ten Brummelaar T A *et al* 2005 First results from the CHARA array: II. A description of the instrument *Astrophys. J.* **628** 453

[7] Nair R and Tsang M 2016 Far-field superresolution of thermal electromagnetic sources at the quantum limit *Phys. Rev. Lett.* **117** 190801

[8] Schermelleh L, Ferrand A, Huser T, Eggeling C, Sauer M, Biehlmaier O and Drummen G P C 2019 Super-resolution microscopy demystified *Nat. Cell Biol.* **21** 72

[9] Lupo C, Huang Z and Kok P 2020 Quantum limits to incoherent imaging are achieved by linear interferometry *Phys. Rev. Lett.* **124** 080503

[10] Pearce M E, Campbell E T and Kok P 2017 Optimal quantum metrology of distant black bodies *Quantum* **1** 21

[11] Howard L A, Gillett G G, Pearce M E, Abrahao R A, Weinhold T J, Kok P and White A G 2019 Optimal imaging of remote bodies using quantum detectors *Phys. Rev. Lett.* **123** 143604

[12] Hanbury Brown R 1968 Stellar interferometer at Narrabri observatory *Nature* **218** 637

[13] Hanbury Brown R and Twiss R Q 1956 A test of a new type of stellar interferometer on Sirius *Nature* **178** 1046

[14] Hanbury Brown R 1974 *The Intensity Interferometer: Its Application to Astronomy* (London: Taylor and Francis)

[15] Mandel L and Wolf E 1995 *Optical Coherence and Quantum Optics* (Cambridge: Cambridge University Press)

[16] Lawson P 2000 *Principles of Long Baseline Stellar Interferometry* (Grand Rapids, Michigan: JPL)

[17] Tan P K, Yeo G H, Poh H S, Chan A H and Kurtsiefer C 2014 Measuring temporal photon bunching in blackbody radiation *Astrophys. J.* **789** L10

[18] Tan P K, Chan A H and Kurtsiefer C 2016 Optical intensity interferometry through atmospheric turbulence *Mon. Not. R. Astron. Soc.* **457** 4291

[19] Zmija A, Deiml P, Malyshev D, Zink A, Anton G, Michel T and Funk S 2020 LED as laboratory test source for astronomical intensity interferometry *Opt. Express* **28** 5248

[20] Matthews N, Kieda D and LeBohec S 2018 Development of a digital astronomical intensity interferometer: laboratory results with thermal light *J. Mod. Opt.* **65** 1336

[21] Naletto G, Zampieri L, Barbieri C, Barbieri M, Verroi E, Umbriaco G, Favazza P, Lessio L and Farisato G 2016 A 3.9 km baseline intensity interferometry photon counting experiment *Quantum Communications and Quantum Imaging XIV* vol 9980 ed R E Meyers, Y Shih and K S Deacon (Bellingham, WA: International Society for Optics and Photonics, SPIE) pp 44–59

[22] Guerin W, Dussaux A, Fouché M, Labeyrie G, Rivet J-P, Vernet D, Vakili F and Kaiser R 2017 Temporal intensity interferometry: photon bunching in three bright stars *Mon. Not. R. Astron. Soc.* **472** 4126

[23] Matthews N and LeBohec S 2019 Astrophysical measurements with the VERITAS stellar intensity interferometer (arXiv:1908.03587)

[24] Matthews N, Clarke O, Snow S, LeBohec S and Kieda D 2018 Implementation of an intensity interferometry system on the StarBase observatory *Optical and Infrared Interferometry and Imaging VI* vol 10701 ed M J Creech-Eakman, P G Tuthill and A Mérand (Bellingham, WA: International Society for Optics and Photonics, SPIE) pp 246–54

[25] Weiss S A, Rupert J D and Horch E P 2018 Stellar photon correlation detection with the Southern Connecticut stellar interferometer *Optical and Infrared Interferometry and Imaging VI* vol 10701 ed M J Creech-Eakman, P G Tuthill and A Mérand (Bellingham, WA: International Society for Optics and Photonics, SPIE) pp 255–61

[26] Klaucke P M, Pellegrino R A, Weiss S A and Horch E P 2020 Toward an imaging capability with the southern Connecticut stellar interferometer *Optical and Infrared Interferometry and Imaging VII* vol 11446 ed P G Tuthill, A Mérand and S Sallum (Bellingham, WA: International Society for Optics and Photonics, SPIE) pp 415–26

[27] Guerin W, Rivet J-P, Fouché M, Labeyrie G, Vernet D, Vakili F and Kaiser R 2018 Spatial intensity interferometry on three bright stars *Mon. Not. R. Astron. Soc.* **480** 245

[28] Rivet J-P *et al* 2020 Intensity interferometry of P Cygni in the H α emission line: towards distance calibration of LBV supergiant stars *Mon. Not. R. Astron. Soc.* **494** 218

[29] Acciari V A *et al* 2019 Optical intensity interferometry observations using the MAGIC imaging atmospheric Cherenkov telescopes *Mon. Not. R. Astron. Soc.* **491** 1540

[30] Abeysekara A *et al* 2020 Demonstration of stellar intensity interferometry with the four veritas telescopes *Nat. Astron.* **4** 1164–9

[31] Dravins D 2016 Intensity interferometry: optical imaging with kilometer baselines *Proc. SPIE* **9907** 99070M

[32] van Cittert P H 1934 Die Wahrscheinliche schwingungsverteilung in Einer von Einer Lichtquelle Direkt Oder Mittels Einer Linse beleuchteten Ebene *Physica* **1** 201

[33] Zernike F 1938 The concept of degree of coherence and its application to optical problems *Physica* **5** 785

[34] Pittman T B, Shih Y H, Strekalov D V and Sergienko A V 1995 Optical imaging by means of two-photon quantum entanglement *Phys. Rev.* A **52** R3429

[35] Belen'kii M S and Holmes R B 2004 Investigation of the Cauchy–Riemann equations for one-dimensional image recovery in intensity interferometry *J. Opt. Soc. Am.* A **21** 697

[36] Fienup J R 1978 Reconstruction of an object from the modulus of its Fourier transform *Opt. Lett.* **3** 27

[37] Fienup J R 1982 Phase retrieval algorithms: a comparison *Appl. Opt.* **21** 2758

[38] Fienup J R and Kowalczyk A M 1990 Phase retrieval for a complex-valued object by using a low-resolution image *J. Opt. Soc. Am.* A **7** 450

[39] Strekalov D V, Kulikov I and Yu N 2014 Imaging dark objects with intensity interferometry *Opt. Express* **22** 12339

[40] Wang W, Chen H, Yuan Y, Han Q, Wang G, Zheng H, Liu J and Xu Z 2018 Ptychographical intensity interferometry imaging with incoherent light *Opt. Express* **26** 20396

[41] Cao S, Kok P, Li P, Maiden A M and Rodenburg J M 2016 Modal decomposition of a propagating matter wave via electron ptychography *Phys. Rev.* A **94** 063621

[42] Armstrong J T, Mozurkewich D, Schmitt H R, Restaino S R and Hindsley R B 2011 Comparing the sensitivities of intensity interferometry and Michelson interferometry *Unconventional Imaging, Wavefront Sensing, and Adaptive Coded Aperture Imaging and Non-imaging Sensor Systems* vol 8165 ed S Rogers, D P Casasent, J J Dolne, T J Karr and V L Gamiz (Bellingham, WA: International Society for Optics and Photonics, SPIE) pp 245–51

[43] Kay S M 1993 *Fundamentals of Statistical Signal Processing* (Englewood Cliffs, NJ: Prentice-Hall)

[44] Tsang M, Nair R and Lu X-M 2016 Quantum theory of superresolution for two incoherent optical point sources *Phys. Rev.* X **6** 031033

[45] Šafránek D 2018 Simple expression for the quantum fisher information matrix *Phys. Rev.* A **97** 042322

[46] Liu J, Yuan H, Lu X-M and Wang X 2019 Quantum Fisher information matrix and multiparameter estimation *J. Phys. A: Math. Theor.* **53** 023001

[47] Napoli C, Piano S, Leach R, Adesso G and Tufarelli T 2019 Towards superresolution surface metrology: quantum estimation of angular and axial separations *Phys. Rev. Lett.* **122** 140505

[48] Genoni M G and Tufarelli T 2019 Non-orthogonal bases for quantum metrology *J. Phys. A: Math. Theor.* **52** 434002

[49] Fiderer L J, Tufarelli T, Piano S and Adesso G 2021 General expressions for the quantum Fisher information matrix with applications to discrete quantum imaging *PRX Quantum* **2** 020308

[50] Sidhu J S and Kok P 2020 Geometric perspective on quantum parameter estimation *AVS Quantum Sci.* **2** 014701

[51] Řeháček J, Hradil Z, Stoklasa B, Paúr M, Grover J, Krzic A and Sánchez-Soto L L 2017 Multiparameter quantum metrology of incoherent point sources: towards realistic superresolution *Phys. Rev.* A **96** 062107

[52] Yariv A 1989 *Quantum Electronics* 3rd edn vol 389 (New York: Wiley)

[53] Guyon O *et al* 1999 The nulling stellar coronagraph: laboratory tests and performance evaluation *Publ. Astron. Soc. Pac.* **111** 1321

[54] Tsang M 2019 Resolving starlight: a quantum perspective *Contemp. Phys.* **60** 279

[55] Paúr M, Stoklasa B, Hradil Z, Sánchez-Soto L L and Rehacek J 2016 Achieving the ultimate optical resolution *Optica* **3** 1144

[56] Tang Z S, Durak K and Ling A 2016 Fault-tolerant and finite-error localization for point emitters within the diffraction limit *Opt. Express* **24** 022004

[57] Yang F, Tashchilina A, Moiseev E S, Simon C and Lvovsky A I 2016 Far-field linear optical superresolution via heterodyne detection in a higher-order local oscillator mode *Optica* **3** 1148

[58] Tham W-K, Ferretti H and Steinberg A M 2017 Beating Rayleigh's curse by imaging using phase information *Phys. Rev. Lett.* **118** 070801

[59] Donohue J M, Ansari V, Řeháček J, Hradil Z, Stoklasa B, Paúr M, Sánchez-Soto L L and Silberhorn C 2018 Quantum-limited time-frequency estimation through mode-selective photon measurement *Phys. Rev. Lett.* **121** 090501

[60] Parniak M, Borówka S, Boroszko K, Wasilewski W, Banaszek K and Demkowicz-Dobrzański R 2018 Beating the Rayleigh limit using two-photon interference *Phys. Rev. Lett.* **121** 250503

[61] Paúr M, Stoklasa B, Grover J, Krzic A, Sánchez-Soto L L, Hradil Z and Řeháček J 2018 Tempering Rayleigh's curse with PSF shaping *Optica* **5** 1177

[62] Hassett J, Malhorta T, Alonso M, Boyd R, Rafsanjani S H and Vamivakas A 2018 Sub-Rayleigh limit localization with a spatial mode analyzer *Laser Science* (Washington: Optical Society of America) pp JW4A–124

[63] Zhou Y, Yang J, Hassett J D, Rafsanjani S M H, Mirhosseini M, Vamivakas A N, Jordan A N, Shi Z and Boyd R W 2019 Quantum-limited estimation of the axial separation of two incoherent point sources *Optica* **6** 534

[64] Cherenkov Telescope Array Observatory gGmbH and CTA Southern Hemisphere Array 2021 https://cta-observatory.org/about/array-locations/chile/ accessed 21 April 2021 CTA southern hemisphere array

[65] Kieda D B *et al* 2019 Astro2020 white paper state of the profession: intensity interferometry (arXiv:1907.13181)

[66] Dravins D, LeBohec S, Jensen H and Nuñez P D 2013 Optical intensity interferometry with the Cherenkov telescope array *Astropart. Phys.* **43** 331

[67] Haubois X and Mieske S 2021 *Very Large Telescope Paranal—Science Operations—VLTI User Manual* European Southern Observatory

[68] Dravins D, LeBohec S, Jensen H and Nuñez P D 2013 Optical intensity interferometry with the Cherenkov telescope array *Astropart. Phys.* **43** 331 seeing the high-energy Universe with the Cherenkov telescope Array—the science explored with the CTA

[69] Nuñez P D, Holmes R, Kieda D, Rou J and LeBohec S 2012 Imaging submilliarcsecond stellar features with intensity interferometry using air Cherenkov telescope arrays *Mon. Not. R. Astron. Soc.* **424** 1006

[70] Wenger M *et al* 2000 The SIMBAD astronomical database *Astron. Astrophys. Suppl. Ser.* **143** 9

[71] Hoffleit D and Warren W H 1995 *Bright Star Catalogue* Centre de Données astronomiques de Strasbourg

[72] Malvimat V, Wucknitz O and Saha P 2013 Intensity interferometry with more than two detectors? *Mon. Not. R. Astron. Soc.* **437** 798

[73] Stee P *et al* 2017 Science cases for a visible interferometer *Research Report* Observatoire de la Côte d'Azur

[74] Nuñez P D and Domiciano de Souza A 2015 Capabilities of future intensity interferometers for observing fast-rotating stars: imaging with two- and three-telescope correlations *Mon. Not. R. Astron. Soc.* **453** 1999

[75] Gottesman D, Jennewein T and Croke S 2012 Longer-baseline telescopes using quantum repeaters *Phys. Rev. Lett.* **109** 070503

[76] Stankus P, Nomerotski A, Složar A and Vintskevich S 2020 Two-photon amplitude interferometry for precision astrometry (arXiv:2010.09100)

[77] Nomerotski A *et al* 2020 Quantum-assisted optical interferometers: instrument requirements *Optical and Infrared Interferometry and Imaging VII* vol 11446 ed P G Tuthill, A Mérand and S Sallum (Bellingham, WA: International Society for Optics and Photonics, SPIE) pp 290–306

[78] Oppel S, Büttner T, Kok P and von Zanthier J 2012 Superresolving multiphoton interferences with independent light sources *Phys. Rev. Lett.* **109** 233603

[79] Rayleigh L 1879 XXXI. Investigations in optics, with special reference to the spectroscope *London, Edinburgh Dublin Phil. Mag. J. Sci.* **8** 261

[80] Pawley J 2006 *Handbook of Biological Confocal Microscopy* (Berlin: Springer)

[81] Goodman J 2005 *Introduction to Fourier Optics* (Greenwood Village, CO: Roberts & Company)

[82] Stein M, Mezghani A and Nossek J A 2014 A lower bound for the Fisher information measure *IEEE Signal Process. Lett.* **21** 796